1982

The Structure of $^{+}$He Ions in Cryogenic Helium Vapor

Gulden Akinci
University of Rhode Island

THE STRUCTURE OF ^{+}He IONS IN CRYOGENIC HELIUM VAPOR

BY

GULDEN AKINCI

A DISSERTATION SUBMITTED IN PARTIAL FULFILLMENT OF THE REQUIREMENTS FOR THE DEGREE OF

DOCTOR OF PHILOSOPHY

IN

PHYSICS

UNIVERSITY OF RHODE ISLAND

1982

DOCTOR OF PHILOSOPHY DISSERTATION

OF

GULDEN AKINCI

Approved:

Dissertation Committee

Major Professor _____

_____

_____

_____

_____

Dean of the Graduate School

UNIVERSITY OF RHODE ISLAND

1982

ABSTRACT

In this research we have studied the structure of ^{+}He ions in He vapor at temperatures between 1.32K - 4.22K and at saturation ratios between 0.05 - 1. Classical macroscopic thermodynamics predicts formation of a liquid drop around the ion, and the drop radius is given by the Thomson equation. In the above temperature and pressure ranges the radius of the drop varies between 6A - 9A. An experimental verification of the Thomson equation shows the validity of the macroscopic thermodynamics when it is applied to microscopic systems and also gives information about the drop structure. To show the existence of the drops and to determine their sizes experimentally, we have measured the mobilities of ^{+}He ions in He vapor in the above temperature and pressure ranges. The mobility is related to the radius of the drop through the momentum transfer cross section. Hence the drop size can be determined from the mobility data if the interaction potential and the nature of collisions between the charged drop and the neutral vapor atom is known. We have assumed that the interaction potential is the sum of the polarization potential between the central ion and the neutral vapor atom, and the van der Waals interactions

between the vapor atom and each of the liquid atoms in the drop. With the above potential the "experimental" drop radius is calculated in the elastic and "inelastic" models. Quantum corrections are made for the elastic model. The Thomson equation predictions were compared with the "experimental" radii and a good agreement was found. This comparison also showed the existence of a solid core within the liquid drop. The classical macroscopic thermodynamics was applied successfully to calculate the solid core radius. Finally, the temperature dependencies of the "experimental" radii showed slight variations from the predictions of the Thomson equation at $T<2.3K$. The deviations reach their maximum at $\sim 1.9K$. The existence of superfluid transition in the liquid helium layer of the ion-solid-liquid complex is suggested as an explanation of the temperature dependencies of the "experimental" radii. The proposed transition temperature is $\sim 1.9K$ and it is broadened up to $\sim 2.3K$. The transition starts when the liquid thickness becomes more than a monolayer.

ACKNOWLEDGEMENT

First of all I would like to express my thanks to my supervisor, Prof.J.A.Northby, for his help and encouragement throughout the past five years. Without his initiation and guidance this work could not have been completed. A second "thank you" goes to Mr. Ed Blais , the machinist of our Physics department, who generously devoted his creative energies towards the improvement of our experimental setup whenever things seemed to go wrong. Prof.K.Hartt guided my work on the quantum mechanical calculations of the cross sections. I am grateful for his eagerness to share his expertise on the subject as well as his time. I also would like to thank my husband for his moral support and help in the preparation of the final form of the manuscript. Lastly, I would like to express my heartfelt thanks for the secretaries of our department, Margaret and Judy, whose warm support usually went beyond the usual definition of secretarial obligations.

This work has been supported in part by the National Science Foundation under grants no. DMR7611111 and no. DMR8024366.

TABLE OF CONTENTS

LIST OF TABLES

LIST OF FIGURES

Figure | Page

1. INTRODUCTION

Classical macroscopic thermodynamics is often used to explain both the homogeneous and the inhomogeneous nucleation of microscopic clusters in gases [1-3]. It has also been applied to understand the structure of ^{+}He ions in liquid helium [4,5]. In both cases the classical theory of nucleation is based on the Thomson equation which was derived about a hundred years ago by J.J.Thomson by using macroscopic thermodynamics [6]. In the case of the inhomogeneous nucleation of polarizable vapor atoms around a positive ion, this equation gives a relationship between the temperature and the pressure of the vapor, and the radius of the droplet formed around the ion in thermal equilibrium with the vapor [2];

$$k\,T\,\ln(P/P_{sat}) = \frac{2\,\sigma_{lv}}{n_l\,R_l} - \frac{\alpha\,e^2}{2\,R_l^4} \qquad (1)$$

where R_l is the liquid drop radius, σ_{lv} is the surface tension of the liquid-vapor interface, n_l is the density of the bulk liquid, α is the atomic polarizability and P_{sat} is the saturated vapor pressure at temperature T. In the derivation one assumes an ideal vapor and an incompressible liquid with nearly unity dielectric constant and a sharp liquid-vapor interface with zero thickness.

There are several reasons to check the validity of the Thomson equation. The main criticism is directed to its application to microscopic systems. For the systems to which the Thomson equation is applied the drop sizes are of the order of angstroms. The application of macroscopic thermodynamics to such small systems is questionable. Also, perhaps the drop structure is not as simple as it is assumed to be in the Thomson equation. First of all the central ion differs from the neutral liquid atoms both in size and in structure. Secondly, a solid core might exist in the drop, as a result of the pressure increase induced by the attractive polarization field of the ion. Finally, in the derivation of the Thomson equation the liquid-vapor interface is assumed to be sharp with zero thickness. This means the curvature dependence of the surface tension is completely ignored. The details of the surface structure might be important especially for microscopic drops where the ratio of the surface area to the volume of the drop becomes large. The Thomson equation does not predict any effect on the drop size resulting from the complex structure of the drop. The radius depends only on the surface tension and the density of the assumed bulk liquid just inside the surface of the drop. A study of the predictions of this equation might give some information about the structure of the drop, ion-atom interactions etc. Furthermore

such microscopic droplets will present a valuable opportunity to study the effect of finite size on the thermodynamical properties of the fluids.

The predictions of the Thomson equation have been tested experimentally for various systems. In these studies different experimental methods have been applied. The measurements which are done with a mass spectrometer are used to obtain the enthalpies and the entropies of successive clustering reactions for water and ammonia about various positively charged ions [7,8]. The results are compared with the theoretical ones which are obtained by utilizing the Thomson equation and its appropriate derivatives. In these systems the cluster sizes are relatively small with less than nine molecules in them. The level of disagreement in the above comparison varies with the kind of ion used in the same vapor, and also with the vapor chosen. In general the Thomson equation is found to be inadequate to describe the ion induced nucleation of such microscopic clusters. Also in cloud chambers the supersaturations required for the homogeneous nucleation of various substances are measured. Because of the difficulty of the technique early experiments gave diverse results. The results of more recent diffusion cloud chamber experiments have been compared with the predictions of the classical nucleation theory which is based on the Thomson equation.

Generally good agreement has been obtained[9,10].

Similar thermodynamical arguments which are used in the derivation of the Thomson equation have been applied by Atkins to determine the size of a solid core formed around a positive helium ion in liquid helium[4]. Atkins model had been tested by measuring the mobilities and the viscosities of the $^{+}$He ions in the liquid helium, and comparing the solid core radius calculated from this data with the predictions of the model. A good agreement was found by using the solid-liquid surface tension as an adjustable parameter[5].

In the work described below we have chosen to study $^{+}$He ions in He vapor mainly because the small surface tension of liquid helium results in relatively large drops. In the temperature range, 1.32K - 4.22K, of this experiment, and for saturation ratios between $\sim$0.05 - $\sim$1.00, the number of atoms are estimated to vary between $\sim$15 - $\sim$150. Hence we should have a reasonable chance to see droplet growth and to compare the results with the predictions of the Thomson equation over a large range of droplet sizes. The analogy with the Atkins model and its experimental verification also played a role in this choice. In addition, the $^{+}$He ion - He vapor system has other advantages: A chemical bond between the ion and the liquid atoms can cause deviations from the Thomson equation predictions[7].

Since helium is an inert gas this possibility is minimized in our system. Also, because of its unusual phase diagram the helium drop is expected to remain liquid even at absolute zero. Furthermore, bulk liquid helium makes a transition from superfluid to normal fluid as the temperature increases above 2.17K. It is hard to believe that a superfluid transition will occur in such a microscopic liquid helium drop, and the Thomson equation predicts no effect of the transition on the drop radius even if it does. Nonetheless, a liquid helium drop has the potential to give us a chance to understand if superfluidity exists in such a microscopic system. As a final practical point, the temperature range of this experiment, 1.32K - 4.22K, is a definite advantage in assuring the cleanliness of the experimental cell. For experiments operating at higher temperatures, undesired vapors and ions in the system are difficult to elemina-te and their existence can create problems in analyzing the data.

While it does not provide the most direct information about the structure of the ion, we have nonetheless chosen to study experimentally the ion mobility. We have done so for two principal reasons: First, because the technique is simple and direct, and capable of quite high accuracy, and second, because the ion remains in thermal equilibrium with the vapor throughout the measurement, as assumed in the Thomson model.

The zero field mobility, μ , of an ion in a gas is defined as;

$$\mu = \lim_{E_d \to 0} \frac{V_d}{E_d} \qquad (2)$$

where V_d is the drift velocity of the ion in an electric field E_d. The mobility is directly related to the momentum transfer between the ion complex and the vapor atoms. Hence experimental momentum transfer cross sections can be calculated directly from the measured mobilities. On the other hand, if the interaction potential between the charged drop and the neutral vapor atom is known as a function of the drop radius, and if a particular scattering model is adopted, then the theoretical momentum transfer cross sections can be calculated for a given radius. The radius for which the theoretical cross section is equal to the experimental cross section obtained directly from the mobility data is taken to be the "experimental" radius of the drop. It should be emphasized that the "experimental" drop radius obtained in this way depends on the scattering model adopted. It gives the actual size of the drop only if the assumed scattering model containes all the features of the collisions between the drop and the neutral atom. Not being able to measure the drop size directly is a disadvantage of the experimental method that we have chosen. But other than their being simple, the mobility experiments have another advantage of maintaining the thermal equilibrium between the liquid drop and the surrounding vapor

during the measurement. For example in a mass spectroscopy experiment the correction has to be made to compensate the effect of evaporation of the liquid atoms from the surface of the drop when the drops are placed in vacuum.

In addition to our previous reports [11-14], there are two more measurements of the mobilities of $^{+}$He ions in He vapor which indicate droplet formation. The first is the a.c. mobility measurement at saturated vapor pressure at 4.2K [15]. This experiment indicated that the effective mass of a positive ion in He vapor was about 75 helium masses but the result could not be reproduced. The second is the d.c. mobility measurements by Henson [16] at temperatures 2.0K - 5.2K and at fairly high pressures. As it will be discussed later, if there is no drop formation and if the vapor is assumed to be ideal, the mobility, μ, should be inversely proportional to the pressure, p. At a constant temperature, Henson interpreted the deviation of $\ln\mu$ versus $\ln p$ graph of his data from a straight line at high pressures as an indication of the droplet growth. However, no attempt was made to obtain quantitative information about the drop sizes. In our preliminary publications we have reported some samples of mobilities at temperatures 1.32K - 4.22K [11-14]. The existence of the drops were shown qualitatively even at low densities. The development of our quantitative analysis can be found in our previous publications. The final form of this analysis will be discussed in section IV of this report. The "experimental"

radii obtained in each model were compared with the predictions of the Thomson equation. Good agreement was found over the entire pressure and temperature range of the experiment.

In this report we extend our calculations of "experimental" radii to include quantum effects. Together with the previous results, these calculations provide us with a deeper insight into the structure of the liquid helium drop. Here, we would like to report the details of the experiment and the results that we have obtained. In the second section the details of the experimental set up and the procedure followed for measurement and the analysis of the raw data will be given. In section III a complete list of the mobilities that we have measured will be given. Their dependence on temperature and pressure will be displayed. The details of the calculations of the theoretical and the experimental radii will be discussed. The last section is reserved for the discussion of the results that we have obtained from the mobility data and from the comparison of the theoretical and the "experimental" radii.

II. EXPERIMENT

The mobilities of $^{+}$He ions are measured by a pulsed time-of-flight method. A schematic of the apparatus is shown in Fig. 1. Ionization is produced by a tritium β-source, S. An electric field causes the positive ions to move toward the gate grid G1. The same electric field applies an opposite force on the primary β particles and prevents them from entering the gate region G1-G2. The drops are formed around the ion in the source region, A. A small potential barrier between G2 and G1 which keeps the positive ions in the source region is overcome by an application of a positive square pulse on the grid G1, and the ions enter and cross the uniform field drift region B. The width of the gate pulse is long enough to create an equilibrium current through the gate G1-G2, i.e., the current created in region B is independent of the width of the G1 pulse. The ions induce a current on the collector, C, as they move from grid G3 to the collector. The electric field in this region is the same as the electric field in the drift region. The time of flight of ions between G2 and C is determined by the time between the cut off of the G1 pulse and the trailing edge of the collector pulse. The mobility of the ions is then calculated from Eq. (2). The grid assembly is placed in a copper can which is filled with helium gas, and surrounded by a liquid helium bath.

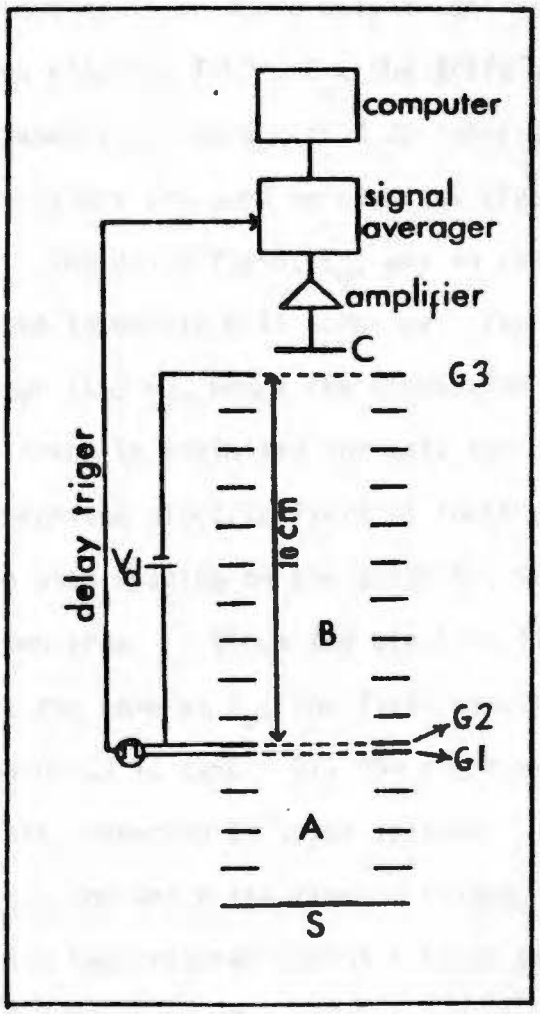

Fig. 1

Schematic of the experimental cell.

The tritium-β source is a tritiated titanium foil with activity 600 m Ci, maximum energy 18 KeV, active area 1.2 x 2 cm^2. The 5.23 cm long source region is long compared to the track length so that ionization is produced only in the source region. To obtain a constant electric field, E_d, the drift space is divided by 9 equally spaced electrodes with 3 cm inner diameter. 10K Ω precision resistors are used between the electrodes as potential dividers. The drift field, E_d, was in the range 8-20 v/cm and was measured to within 0.1% accuracy. The diameter of the guarded collector is 2 cm, hence the distortion of the electric field near the collector is minimized and only the central portion of the ion beam, where the electric field is least distorted, is collected. The wire spacing on the grids G1, G2 and G3 is 0.05 cm with 85% open area. Since the electric field in the collector region is the same as E_d, the field penetration due to the grid spacing on G3 is zero. All the electrodes, grids, and the collector are connected by lexan spacers. The total distance from G2 to C for which the time of flight is measured is 10.50 cm at helium temperatures (G2-G3 = 10.00 cm, G3-C = 0.50 cm). This length is calculated from room temperature measurements of the same length and the known expansion coefficient of the spacers. To prevent oxidation, the stainless steel electrodes, grids, collector and source support are gold plated. To assure cleanliness the system is evacuated up to $\sim 1 \times 10^{-4}$ torr before

each run. A small amount of pure helium exchange gas is admitted into the can through a liquid nitrogen cooled charcoal trap at the beginning of the run. Otherwise during the experiment only the boil off from liquid helium in the bath is used to increase the can pressure.

A. Drift time measurements

The 10^{-10} - 10^{-11} A/cm^2 current pulses, received by the collector are amplified by a current amplifier in which an Analog Device 41J operational amplifier is used with 10^9 Ω feedback resistor, R_c. The signal to noise ratio (~7) of the current amplifier is low enough so that the amplifier did not create any problem in finding a recognizable pulse, and after the signal averaging, the uncertainity due to amplifier noise was always negligible compared to the errors due to diffusion, space charge etc. The 0.36 msec time constant, τ, of the amplifier is uncertain by about ± 0.10 msec. To increase the accuracy a delayed trigger was used for the signal averager, and only the trailing edge of the amplifier output was averaged. The digital signal averager was operated so that its resolution was not a limiting factor. Its output was stored in a computer to be analyzed later. The drift time of the ions was found by the following procedure: The output voltage, V(t), is related to the input current, i(t), for an idealized current amplifier by $i(t) = 1/R_f \left(V(t) + \tau \, dV/dt \right)$ where τ is the feedback time constant.

We eliminate the effect of the time constant by calculating i(t) directly from the data on a point by point basis, using the experimental value of τ. Because of the dV/dt term in this equation the new pulses appear to be noisier. The deconvoluted pulses with four different amplitudes for the same drift field are shown in Fig. 2. The rounding of the edges is due to diffusion and the wire spacing on the grid G2 only since there is no field penetration on G3 as mentioned before. The times t_1 and t_2 are the intercepts of the tangent line with the lines defining the amplitude of the pulse. Ideally as the trailing edge of the pulse moves across the collector region the current goes linearly to zero. Hence the response defined by lines A, B and T is probably very close to the ideal response. Since t_2 is more accurately defined, it is preferred over t_1 and added to the delay time to find the total time of flight τ_d. As mentioned before the corresponding drift length, L, is 10.50 cm from the grid G2 to the collector. $t_2 - t_1$ is the time passed for the ions at the trailing end of a pulse to travel through 0.5 cm collector region. Therefore for each pulse $(t_2 - t_1) / \tau_d$ must be $\sim$0.048. This is consistent with our observations.

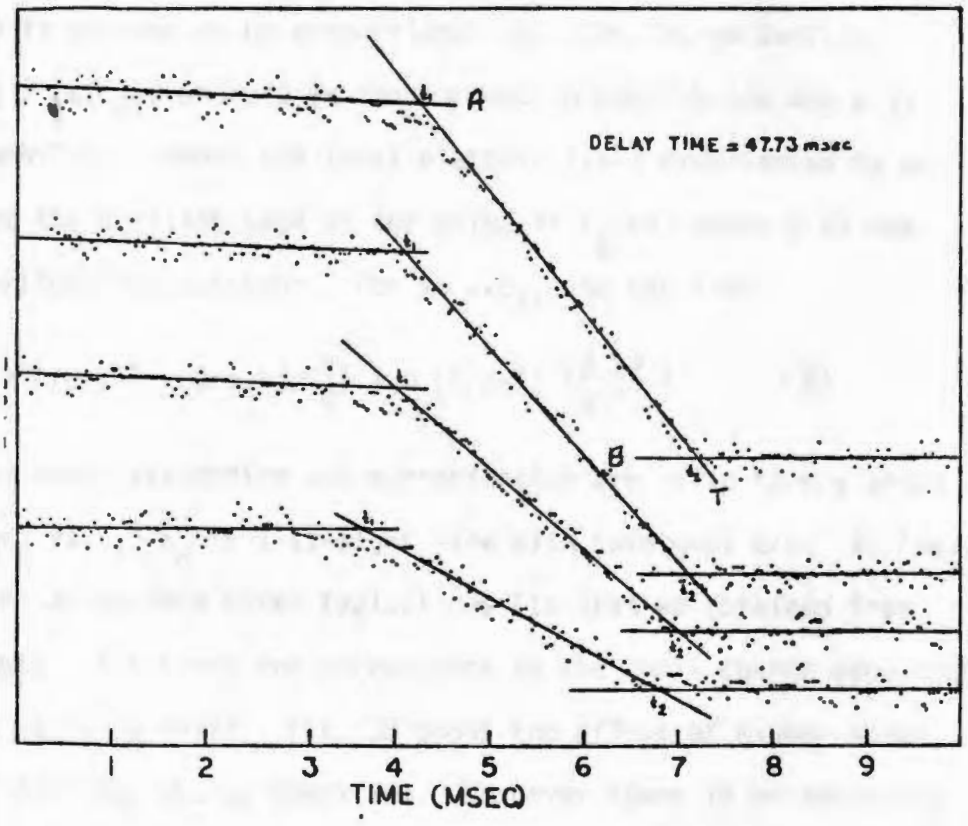

Fig. 2

The deconvoluted pulses with four different amplitudes.

Four different pulse amplitudes were chosen for each drift field E_d to determine the effect of space charge on the transit time. In Fig. 2 the different values of the intercept , t_2 , for each pulse amplitude show the magnitude of this effect. We compensate for the space charge effect by the following argument: Each ion in the drift region experiences an additional electric field resulting from the other charges around it. This electric field is assumed to be proportional to the charge density $n = j / (e\mu E_d)$, where j is the current in equilibrium and μ is the mobility. Hence the total electric field experienced by an ion at the trailing edge of the pulse is $E_d - Kn$, where K is the proportionality constant. For $Kn \ll E_d$, one can find:

$$E_d \tau_d = L/\mu \{ 1 + K/e\mu(j/E_d^2) + 0 [K/e\mu(j/E_d^2)]^2 \} \qquad (3)$$

If the above assumption and approximation are valid then a graph of $E_d\tau_d$ vs. j/E_d^2 is a straight line with intercept L/μ. In Fig. 3a, 3b, 3c we show three typical results that we obtained from our data. The first one corresponds to the small charge densities where Eq. 2 is valid. Fig. 3b shows the effect of higher order terms for high charge densities. Whenever there is an ambiguity due to lack of data at small charge densities, as shown in Fig. 3c, we took the value of $E_d\tau_d$ at the mid-point of the intercept 1 and and the intercept 2 to calculate the mobility. For these cases we assign larger uncertainity to include both of the intercepts.

It should be noted that the magnitude of these corrections are only about ∿1% of the measured transit times.

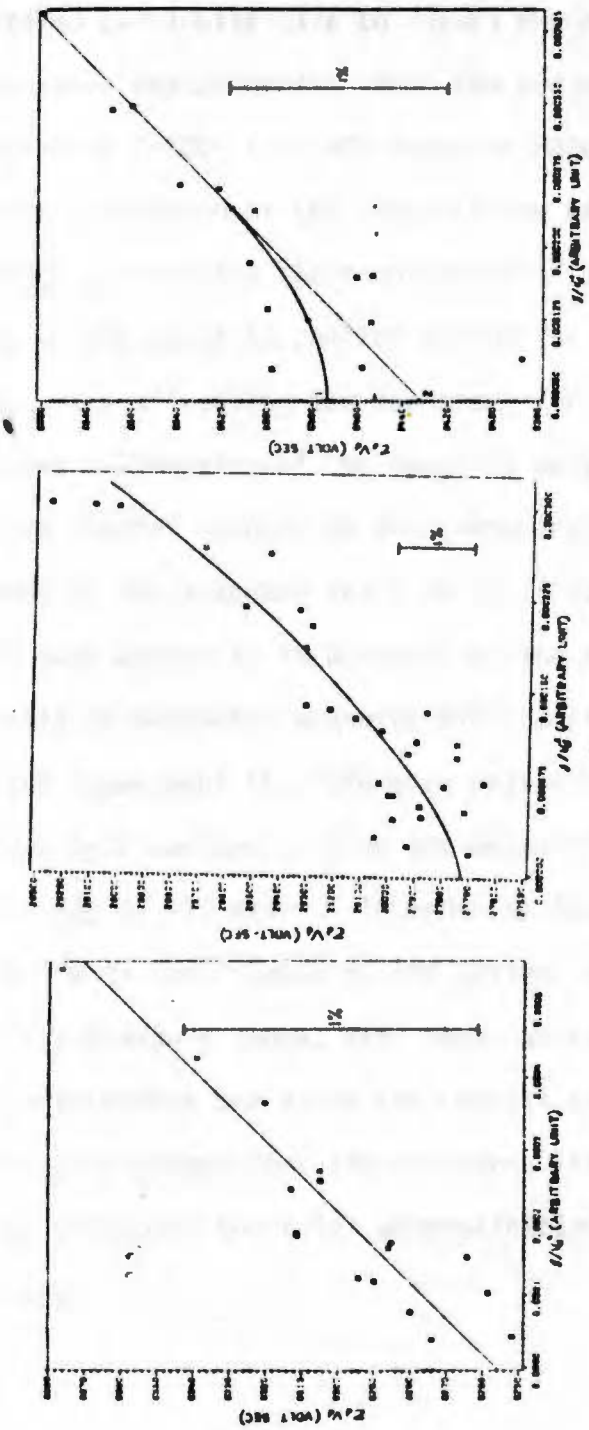

Fig. 3A Fig. 3B Fig. 3C

Three typical results of the space charge effect. The terms are explained in the text.

B. Pressure and temperature measurements

Since the mobility is a sensitive function of vapor density we have taken particular care to insure the accuracy of our pressure and temperature measurements. Both the can and the bath pressures are measured by 0-1000 torr MKS Baratron Model 170 capacitance manometer. The connection of the gauge to the experimental chamber is large enough to make the thermomolecular effects negligible. The linearity of the gauge is checked against an oil manometer within the 1% accuracy of reading the manometer for pressure 5-40 torr. The pressure calibration of the gauge is made by measuring the pressure at λ-point transition and comparing the value that the gauge reads to the standard value of 37.76 torr. The two are found to be the same within $\pm$0.1% accuracy of the calibration. In fact the capacitance manometer measures differential pressure, and in the present experiment the reference pressure (of about 20 mtorr) is provided by a mechanical pump and measured by a thermocouple to an accuracy of $\pm$10 mtorr. In order to determine the pressure variation due to small leaks in the system, bath temperature drifts, drift of the pressure gauge, etc, each can and bath pressure was measured both before and after the transit time measurements at this particular temperature and pressure. For the highest and the lowest can pressures the total uncertainities are 0.3% and 0.8% respectively.

The temperature of the system is determined from the bath vapor pressure. The coarse temperature regulation is obtained by controlling the pumping speed on the bath. For fine temperature regulation an uncalibrated Ge resistor, in an a.c. bridge circuit, is epoxied on top of the can, and used with a $\sim 100\ \Omega$, $\sim 4 \times 10^{-2}$ W heater in a feedback circuit. Below the superfluid transition temperature, the heater resistor is placed on top of the can. Above this temperature, a chromel wire heater is wrapped around the can to maintain constant temperature through the experimental cell. Also a bellows manostat is used to control the bath pressure at higher temperatures. Above 3K only a needle valve was more practical to keep the bath pressure constant to within 1% accuracy. In this way we could keep the uncertainities in the temperature within 0.08% and 0.24% below and above the λ-point temperature respectively.

C. Error analysis

Most of the uncertainty in the mobility is due to the time of flight measurements. It originates basically from two sources: 0.1 msec uncertainty in the amplifier time constant, and 0.05% - 1% ambiguity in determining the effect of space charge as explained previously. All the other errors in τ_d, created by other sources, are negligible compared to the above two. The uncertainty in the drift field is 0.1%. The random error in the drift length, L, is assumed to be zero. The total uncertainty in almost all mobilities varies between 0.2% to 1.6%. A few of our mobilities have errors

up to 3.8% however.

Uncertainties in the pressure and the temperature are discussed in the previous section. Briefly, they are 0.3% - 0.8% and 0.8% - 0.24% in the pressure and in the temperature respectively.

In the above error analysis the systematic errors in the drift length arising from the uneven drift field, grid spacing etc. are not considered. These uncertainties were discussed in some detail by Schwarz[17] who had measured the mobilities of $^{+}$He ions in liquid helium. To compare our method of measurement and analysis with his and particularly to estimate the possible systematic errors in the drift length, we filled the can with liquid He and measured the $^{+}$He ion mobility at T=1.289K and T=1.257K. The two results at both of the temperatures are consistent with each other within 2% accuracy of Schwarz. Therefore no calibration of effective drift length has been done.

The temperature and the pressure range of this experiment overlaps with those of Henson[16] at temperatures between 2.0K - 4.2K and at high densities. Henson assigned 3% uncertainty in his mobilities. We compared our results with his in this overlapping region of the temperature and the pressure. Our mobilities are slightly higher than his at low temperatures. This disagreement decreases from 15% to 4% as the temperature increases from 2.0K to 3.0K. At higher temperatures the two results are consistent with each other within the mutual error bars.

III. EXPERIMENTAL RESULTS

The temperature range of this experiment is 1.32K - 4.22K. For each temperature, the mobilities are measured for different vapor pressures. The lowest can pressure was about 1 torr. This limit was chosen to keep the uncertainty in pressure within ∿1%. Also we have observed the effect of ionization in the drift region at low vapor densities. The highest can pressure corresponds to a density $\sim 7 \times 10^{19} cm^{-3}$. For higher densities the distortion of the current pulse associated with long transit time made it impossible to make accurate measurements. At these high densities a shorter drift space is necessary. The experimental values of the mobility for each temperature and pressure chosen are tabulated in Table 1.

Table 1.

The mobilities of the ions in He vapor.

T=1.3239K , p_{sat}=1.391 torr		T=1.4278K , p_{sat}=2.495 torr	
p(torr)	$\mu(cm^2/sec\text{-}volt)$	p(torr)	$\mu(cm^2/sec\text{-}volt)$
1.385	21.08	2.418	12.72
1.034	30.09	2.124	14.92
0.890	35.92	1.846	17.69
0.720	45.81	1.520	22.58

T=1.4287K , p_{sat}=2.495 torr (continue...)

p(torr)	μ(cm^2/sec-volt)
1.222	28.86
1.218	29.01
0.863	43.41
1.654	20.10

T=1.5434K , p_{sat}=4.421 torr

p(torr)	μ(cm^2/sec-volt)
2.380	15.58
3.252	10.63
4.179	7.78
0.804	53.76
1.512	26.33

T=1.6555K , p_{sat}=7.181 torr

p(torr)	μ(cm^2/sec-volt)
7.015	4.78
4.884	7.57
2.809	14.60
0.882	53.78

T=1.7615K , p_{sat}=10.847 torr

p(torr)	μ(cm^2/sec-volt)
1.763	28.76
3.475	12.92
5.100	8.18
6.829	5.74
8.394	4.47
10.427	3.39
9.470	3.81
5.850	6.93
2.945	15.63
5.459	7.58

T=1.8735K , p_{sat}=16.030 torr

p(torr)	μ(cm^2/sec-volt)
2.050	25.63
6.080	7.50
10.800	3.76
13.500	2.87
9.023	4.69
4.007	12.11

T=2.0009K , p_{sat}=23.83 torr

p(torr)	$\mu(cm^2/sec\text{-}volt)$
14.270	3.17
10.170	4.68
6.190	8.38
2.020	28.72
18.050	2.37
22.240	1.95
20.665	1.95
5.672	9.23
7.357	6.81
16.170	2.66

T=2.1704K , p_{sat}=37.660 torr

p(torr)	$\mu(cm^2/sec\text{-}volt)$
3.066	20.55
7.933	7.22
0.971	68.47
14.967	3.43

T=2.2995K , p_{sat}=50.960 torr

p(torr)	$\mu(cm^2/sec\text{-}volt)$
15.851	3.62
20.187	2.73
13.527	4.31
2.668	25.50
1.057	67.30
18.220	3.06
15.020	3.97
9.960	6.08
5.130	12.65

T=2.5250K , p_{sat}=81.375 torr

p(torr)	$\mu(cm^2/sec\text{-}volt)$
9.796	7.18
6.503	11.11
6.383	11.40
4.919	14.96
0.949	82.99
12.566	5.51
17.425	3.77
33.080	1.789
24.730	2.513

T=3.0340K , p_{sat}=191.50 torr

p(torr)	μ(cm^2/sec-volt)
31.086	2.59
21.051	4.04
11.488	7.78
6.290	14.23
25.050	3.46
1.059	92.41
15.360	5.75
22.962	3.74
25.102	3.40
5.003	18.49
1.926	50.32

T=4.2230K , p_{sat}=765.7 torr

p(torr)	μ(cm^2/sec-volt)
5.422	25.88
10.373	12.84
20.220	6.59
31.750	4.06

T=3.5020K , p_{sat}=356.7 torr

p(torr)	μ(cm^2/sec-volt)
12.337	8.57
1.053	112.50
26.580	3.77
20.520	4.78
14.438	7.30
7.575	14.11
28.570	3.58

The reduced mobility μ_r is defined as

$$\mu_r = \mu \frac{n}{n_{ref}} \qquad (4)$$

where $n_{ref}=2.69 \times 10^{19}$ cm^{-3} and n is the vapor density calculated by the virial equation of state[18]. The reduced mobility is displayed as a function of saturation ratio for several temperatures and as a function of temperature for several saturation ratios in Fig. 4 and Fig. 5 respectively.

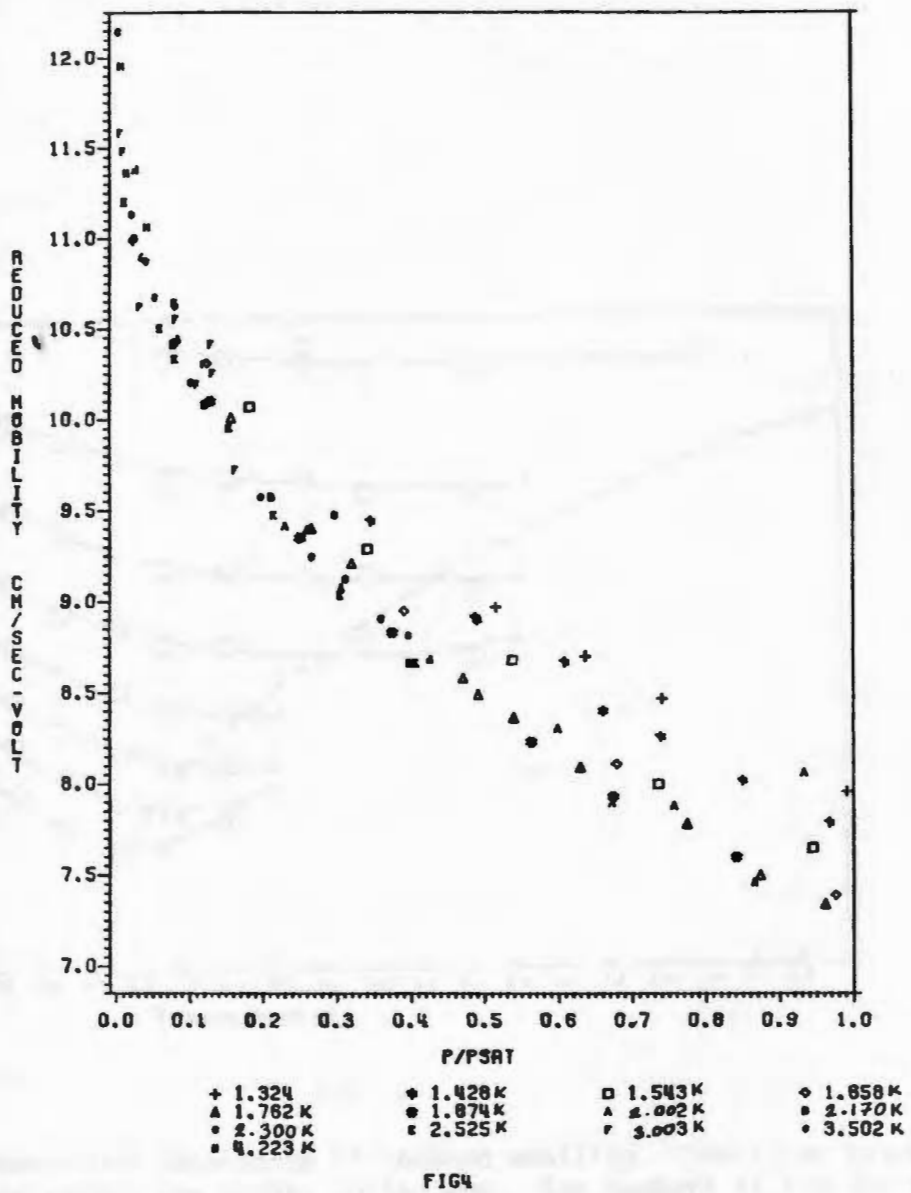

FIG4

The dependence of reduced mobility on the saturation ratio. Different symbols correspond to different temperatures.

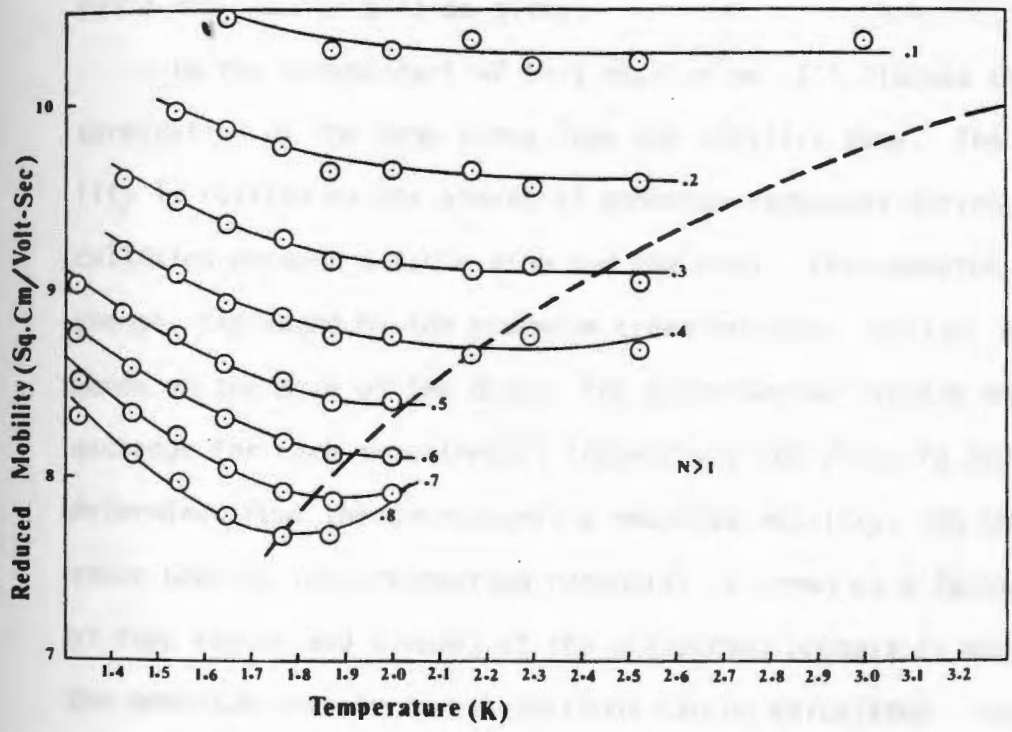

Fig. 5

The temperature dependence of reduced mobility. The lines between the data points are guides to the eye. The numbers at the end of the lines show different saturation ratios. The dashed line shows the "boundary" between the binary and multiple collision regimes.

IV. THEORY AND CALCULATIONS

In the first part of this section we will explain the calculation of the theoretical drop radius predicted by the Thomson equation. Some modifications that we have made to this equation will be discussed. Also the possibility of formation of a solid core inside a liquid drop and its effect on the drop radius will be introduced. The theoretical determination of the solid core radius will be given.

In the second part of this section we will discuss the determination of the drop sizes from the mobility data. The mobility is related to the amount of momentum exchanged during a collision between a vapor atom and the drop. The momentum exchange, expressed by the momentum transfer cross section, depends on the size of the drop. The experimental average momentum exchange for each experimental temperature and pressure can be determined from the corresponding measured mobility. On the other hand if the interaction potential is known as a function of drop radius and a model of the scattering process is adopted, the momentum transfer cross sections can be calculated. Hence for each scattering model there is an "experimental" drop radius which corresponds to the experimental momentum transfer cross section. These "experimental" drop radii depend not only on the scattering model but also on the mechanics of the scattering process. Depending on the temperature and the size of the drop,

quantum mechanical calculations of the momentum transfer cross sections might give different radii than the classical ones. In this second part of this section, the determination of the "experimental" drop radius in two different scattering models and the quantum effects on these calculations will be discussed. It should be emphasized that probably none of these model dependent "experimental" radii reflect the precise size of the drop, but nonetheless they are helpful in understanding some features of the drop structure.

A. Thomson equation's predictions

The theoretical drop radius, R_1, is determined by the Thomson equation (Eq. 1) for each experimental temperature and pressure. Measured values for the bulk surface tension, $\sigma_{1v}(T)$[19], liquid density, $n_1(T)$[20], and α=0.205 A^3[21] are used in these calculations.

The usual derivation of the equation presumes that the vapor is ideal. We also tried a version modified to include the non-ideal behavior of the vapor, but no appreciable effect on radius could be found. The derivation also neglects any density variations within the drop and any dependence of the surface tension on curvature. Since the pressure inside the liquid increases toward the center of the drop due to the polarization attraction between the ion and the liquid He atoms,

it is reasonable to argue that the liquid density increases over the bulk liquid density as the distance from the ion decreases. Also the surface tension of the liquid-vapor interface of the finite size drop is different from, probably smaller than, the bulk surface tension [22]. Hence one can speculate that the (σ_{lv}/n_l) ratio in Eq.1 is smaller than its bulk value. To understand how sensitive is the drop radius to decreasing the σ_{lv}/n_l ratio we have calculated R_l in Eq. 1 for $\sigma_{lv} / n_l = (8/10)(\sigma_{lv}/n_l)_{bulk}$. This choice of the σ_{lv}/n_l ratio increased the drop radius for all temperatures and pressures by about 5-6% [14], but the results did not change any of the conclusions that we will discuss in the following section. Therefore they will not be included in our discussion. The theoretical drop radius is then given by Eq. 1 with no modifications.

The pressure increase in the drop due to the polarization force should not only increase the liquid density but it should also result in a solid core inside the liquid drop [4,5]. The Thomson equation does not predict any effect of the solid core on the drop radius. In fact the drop radius is completely independent of the structure inside. But it depends on the bulk liquid density just inside the drop surface and the surface tension. Hence as long as the existence of the solid core does not effect the density of the liquid layer and the surface tension,

the drop radius should remain constant. But for sufficiently small drops the solid-liquid interface might be very close to the liquid-vapor interface such that the solid core might have an effect on the properties of the liquid-vapor surface and of the liquid layer. The solid core radius, R_s, is calculated by using the similar thermodynamical arguments which are used in the derivation of the Thomson equation. It is given by

$$k\,T\,\ln(p/p_{sat}) - p_m/n_l = 2\,\sigma_{sl}/(n_s-n_l)R_s - \alpha e^2/2R_s^4 \qquad (5)$$

where p_m is melting pressure, n_s is the density of the solid, and σ_{sl}=0.1 dyne/cm is the solid liquid surface tension[23]. In the above equation the solid is assumed to be incompressible with nearly unity dielectric constant. Equations 1 and 4 are used to calculate the liquid and the solid radii. The measured values of bulk $p_m(T)$ and $n_s(T)$ are used in these calculations[20]. The effects of the solid core on the drop size as liquid thickness, R_l-R_s, decreases will be discussed in the following section.

B. Model dependent "experimental" radii

As mentioned before the mobility is not directly related to the size of the drop but it is related to the momentum transfer cross section. In Chapman Enskog theory the relationship between the reduced mobility, μ_r, and a thermally averaged momentum transfer cross section, $\Omega^{(1,1)}$, is given by[24]

$$\mu_r = (3e/16n_{ref})(2\pi/m_r kT)^{1/2} / \Omega^{(1,1)} \qquad (6)$$

where m_r is the reduced mass, indistinguisable from the mass of a single helium atom in the present case. The above equation is valid only for elastic, binary collisions but in some cases it can also be applied to inelastic collisions [24,25]. We used Eq. 5 to calculate the experimental cross sections $\Omega^{(1,1)}_{exp}$ from the measured values of the mobility.

On the other hand, if the interaction potential between the charged drop and the neutral vapor atom is known for a given drop size, we can adopt a model describing the nature of scattering and calculate thermally averaged momentum transfer cross sections theoretically for any drop size. Then for each model an "experimental" drop radius for which $\Omega^{(1,1)}_{th} = \Omega^{(1,1)}_{exp}$ can be found.

In the calculation of the theoretical cross sections we assumed that the interaction potential is the sum of the $-C/r^4$ polarization potential between the central charge on the vapor atom, and the van der Waals potential, $-C_6/r^6 + C_{12}/r^{12}$, between the vapor atom and each of the neutral atoms in the liquid. If the density of the liquid is assumed to be constant, integrating the latter over the volume of the drop gives

$$V(r)=-C/r^4 - AR^3 \left[C_6 \frac{1}{(r^2-R^2)^3} - C_{12} \frac{15r^6+63R^2r^4+45R^4r^2+5R^2}{15(r^2-R^2)^9} \right] \quad (7)$$

where $C \equiv \alpha e^2/2$, $A \equiv 4\pi n_1/3$, $C_6 = 1.139 \times 10^4 K\text{-}A^6$, $C_{12} = 3.1778 \times 10^6 K\text{-}A^{12}$ and R is the drop radius which is chosen as an adjustable parameter[26].

To calculate the transport cross section, $Q^{(1)}$, from the above potential we have adopted two different scattering models.

1. Elastic scattering model: In this model we assumed that all the collisions are elastic. In this case the problem is well defined both in classical and in quantum mechanical approach. In the classical case $Q^{(1)}$ is defined by

$$Q^{(1)}(E) = 2\pi \int_{r_a}^{\infty} (1-\cos\Theta)\, b\,db \quad (8)$$

where b is the impact parameter, E is the relative energy of the incident atom. The scattering angle Θ is given in terms of b as

$$\Theta(b) = \pi - 2b \int_{r_a}^{\infty} [1-b^2/r^2-V(r)/E]^{-1/2}\, dr/r^2 \quad (9)$$

where r_a, the distance of closest approach, is the outermost root of $1-b^2/r_a^2-V(r_a)/E=0$ and V(r) is the interaction potential given by Eq. 7. The transport cross section $Q^{(1)}$ is calculated by numerical integration of Equations 8 and 9.

To be able to include this type of scattering in our model we assumed that every atom which "touches" the drop is absorbed by the drop and simultaneously another atom is emitted in a random direction but with the same energy so as to maintain the thermal equilibrium. Furthermore we assumed that an atom "touches" the surface if its classical distance of closest approach is less that r_m, the position of the minimum of the potential V(r). All the other atoms which do not "touch" the surface are assumed to be scattered elastically. We call this model the "inelastic" model. Only classical mechanics is used in these calculations. For elastically scattered atoms ($r_a > r_m$), $Q^{(1)}$ are calculated from equations 8 and 9. Because the scattering angle, θ, is assumed to be random for atoms with $r_a \leq r_m$, $\ll Cos\theta >= 0$. Hence $1-Cos\theta = 1$ is substituted into Eq.8 if $r_a \leq r_m$.

As mentioned before to estimate the "experimental" radii within each model, the thermally averaged momentum transfer cross section, $\Omega^{(l,1)}$, must be calculated. The relationship between $\Omega^{(l,1)}$ and $Q^{(l)}$ is defined as;

$$\Omega^{(l,1)}(T) \equiv [1/2(kT)^3] \int_0^\infty \exp(-E/kT) E^2 Q^{(l)}(E)\, dE \qquad (11)$$

where E is the relative energy of the incident atom. The transport cross sections calculated in each model are used in Eq.11 to determine $\Omega^{(l,1)}_{th}$ for given drop radii, R. The value of R for which $\Omega^{(l,1)}_{exp} = \Omega^{(l,1)}_{th}$ is taken as the "experimental"

drop radius for each model. The uncertainty in the "experimental" radii due to the above calculations alone are 0.4%, 1% and 0.4% for the elastic classical, the elastic quantum mechanical and the inelastic cases respectively. For the details of these calculations see Appendix C.

In Fig.6 the three different "experimental" radii are displayed as functions of saturation ratio at T=1.762K. R_{ce} and R_e represent the "experimental" radii determined from the classical and the quantum mechanical elastic scattering model calculations. R_i is the "experimental" radius predicted from the inelastic scattering model. Most probably none of these "experimental" radii reflect the true size of a drop. The elastic model ignores the effects of inelastic collisions which are dominant at least for the case of the scattering of the He atoms from the bulk liquid surface. The "inelastic" model on the other hand ignores quantum effects. Besides the type of "inelasticity" chosen may not be the case for the real system under consideration. Despite of the differences in their determination, however, R_{ce}, R_e and R_i have the same functional dependence on saturation ratio. Their ratio to each other is almost constant over all the temperature and the pressure range. The difference between the three "experimental" radii is at most 3A. This suggests that a more realistic model

which includes both the true inelastic and the quantum nature of the scattering would probably give results close to our present estimations also. Comparisons of R_{ce} and R_i, R_{ce} and R_e show that both inelasticity and quantum effects lower the estimated "experimental" drop radius. Hence the result of such a more realistic model is expected to be slightly smaller than all of the "experimental" radii displayed in Fig.6. In the following section we will compare the "experimental" radii with the theoretical drop radius, R_1, predicted by the Thomson equation. In this comparison we will include only R_e to represent the elastic model, because it contains the quantum effects and therefore is more realistic than R_{ce}.

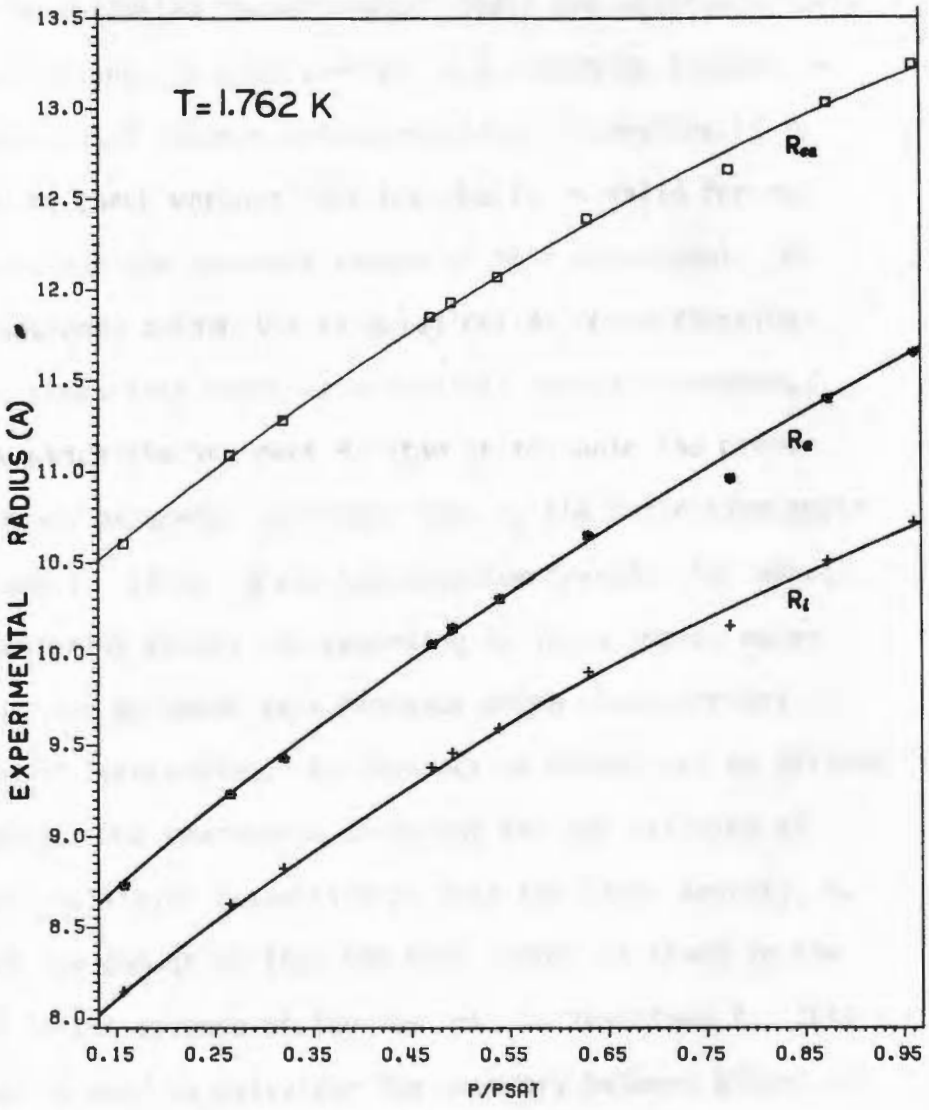

FIG 6

The dependence of the "experimental" radii on saturation ratio. The solid lines through the data points are guides to the eye.

Since the experimental cross sections are obtained from the measured mobilities by using the Chapman Enskog equation (Eq.6), the estimated "experimental" radii are meaningful only if the collisions are binary which is a condition assumed in the derivation of Chapman Enskog equation. Therefore it is necessary to check whether this hypothesis is valid for the temperature and the pressure ranges of this experiment. As it was mentioned before the calculations of the deflection angle, Θ, shows that there is a critical impact parameter, b_c, below which the incident He atom spiral onto the drop. If the impact parameter is bigger than b_c the deflection angle is very small. If we ignore the momentum transfer for small angle scattering events corresponding to large impact parameters, b_c can be taken as a distance which characterizes the range of interaction. An interaction volume can be defined as $V=4\pi b_c^3/3$. One reasonable criterion for the validity of the binary collision assumption is that the vapor density, n, should be low enough so that the mean number of atoms in the volume V in the absence of the ion, nV, is less than 1. This criterion is used to calculate the boundary between binary and multiple collisions for each temperature and pressure. This boundary is displayed in Figures 4 and 5 as dashed lines. It is clear from these figures that almost all of our data is within the binary collision regime.

V. DISCUSSION

In this section we will first make a qualitative analysis of our data. This analysis is independent of any model adopted and it shows the existence of the drops. Then we will compare, quantitatively, the model dependent "experimental" radii with the theoretical radius predicted by the Thomson equation. This comparison enables us to check the validity of macroscopic thermodynamics when it is applied to such a microscopic system and it also provides information about the structure of the microscopic helium drops.

Qualitatively, the existence of a drop formed around the $^{+}$He ion can be seen from the pressure dependence of the reduced mobility, μ_r, at a constant temperature. If the collisions are binary and the temperature is constant, the momentum transfer cross section, $\Omega^{(1,1)}$, should not vary with changing pressure if there is no drop formation. Since the only pressure dependence of μ_r is through $\Omega^{(1,1)}$ (Eq.6), under these conditions, μ_r should also remain constant as the pressure of the system varies. The saturation ratio dependence of the reduced mobility is shown in Fig. 4. The dashed line is the binary-multiple collision "boundary" (see the previous section). Above this line the collisions are mostly binary. The decrease in μ_r in the binary collision regime as p/p_{sat} decreases indicates the momentum

transfer cross section depends on the pressure which means that the drops are indeed growing around the ions. It should be emphasized that this qualitative confirmation of the Thomson equation is independent of any scattering model adopted.

To be able to make quantitative comparisons, the model dependent "experimental" radii are determined by the model explained in the previous section. In Fig.7 and Fig.8 these "experimental" radii, R_e and R_i, and the theoretical radius R_ℓ are displayed as functions of saturation ratio at T=1.428K, and as functions of temperature at p/p_{sat}=0.3 respectively. As can be seen from these figures, the theoretical drop radius is in good agreement with the drop radii, R_e and R_i, estimated from the elastic and "inelastic" scattering models. In fact, for all the temperatures and pressures chosen in this experiment, the disagreement never exceeds 3.0 A which is roughly equal to the diameter of a single He atom (2.2A)[20]. In previous section we have concluded that a more realistic model which includes both the inelastic and the quantum nature of the scattering should not give drastically different results to alter the present good agreement. On the contrary an "experimental" radius which is estimated by such a model is likely to be smaller than both R_e and R_i and thus probably be closer to the theoretical radius R_ℓ. Therefore we conclude that the Thomson equation predicts the drop radii reasonably accurate for all the drop sizes that we have in the temperature and pressure ranges of

this experiment.

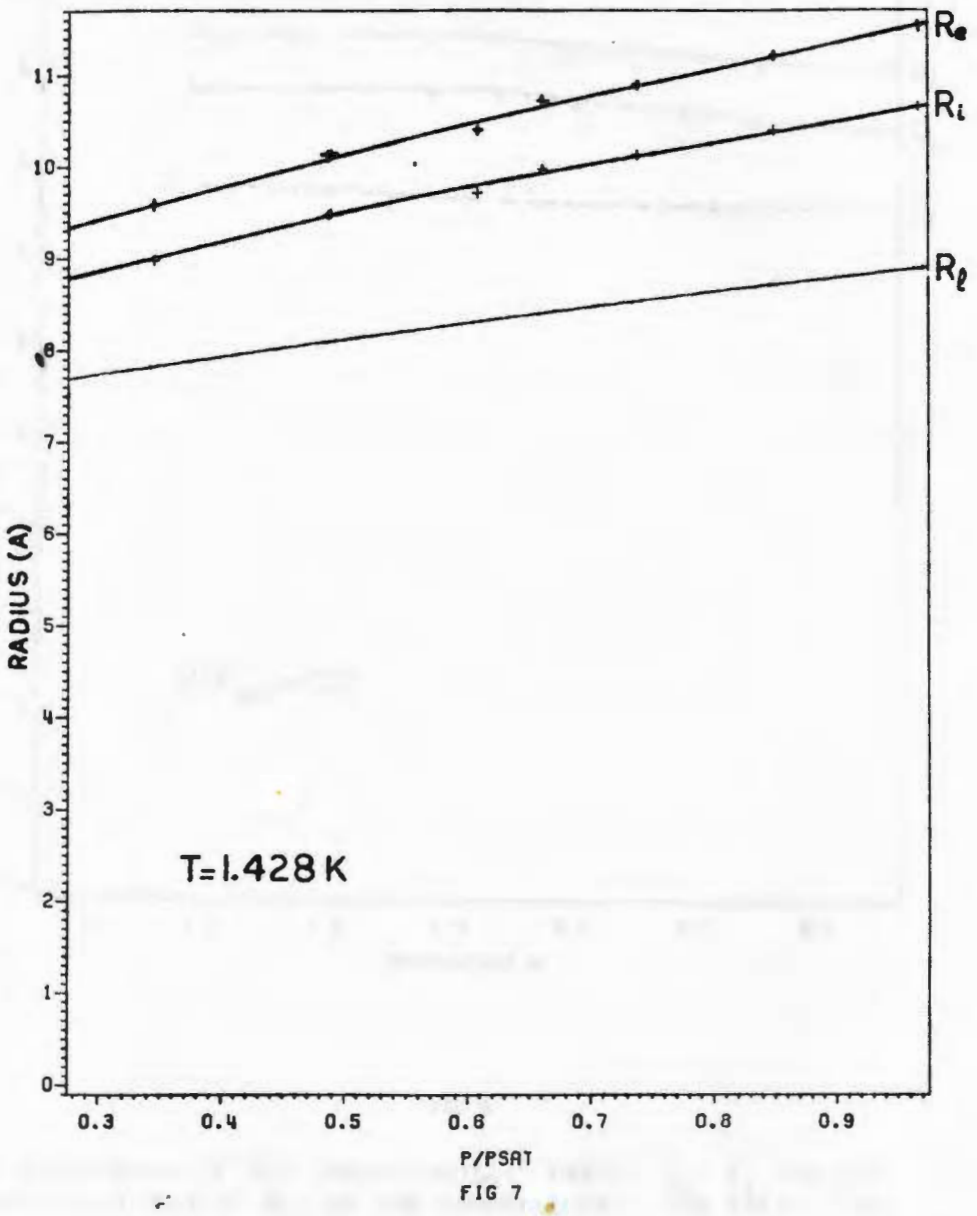

FIG 7

The dependence of the "experimental" radii, R_e , R_i and the theoretical radius R_l on the temperature. The solid lines through the data points are guides to the eye.

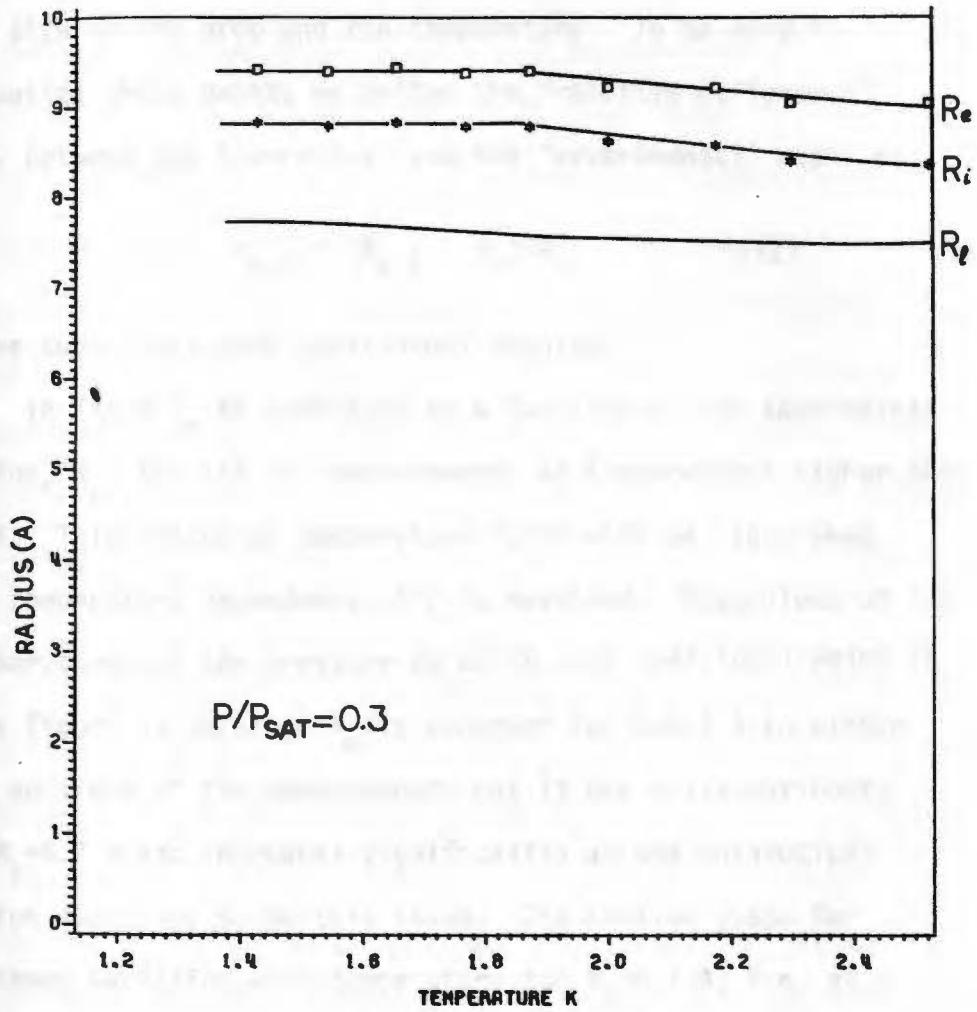

FIG 8

The dependence of the "experimental" radii, R_e, R_i and the theoretical radius R_l, on the temperature. The solid lines through the data points are guides to the eye.

The small difference between the theoretical and the "experimental" radii shows interesting dependencies both on the size of the drop and the temperature. To be able to emphasize these points we define the "relative difference", δ, between the theoretical and the "experimental" radii as;

$$\delta_{e,i} = (R_{e,i} - R_\ell)/R_\ell \qquad (12)$$

where subscripts have their usual meaning.

In Fig.9 δ_e is displayed as a function of the theoretical radius, R_ℓ, for all our measurements at temperatures higher than 2.3K. This choice of temperature range will be clear when the temperature dependence of δ is examined. Regardless of the temperature and the pressure at which each individual point in this figure is obtained δ_e is constant for R>6.7 A to within the accuracy of the measurements but it has a discontinuity at R_ℓ=6.7 A and increases significantly as the theoretical radius decreases below this value. The similar graph for δ_i shows variation with temperature for R_ℓ<6.7 A, i.e. at a constant temperature δ_i decreases with increasing R_ℓ, but the value of δ_i is bigger at lower temperatures at a constant value of R_ℓ. For R_ℓ>6.7 A the variation of δ_i with temperature no longer exists, and like δ_e, δ_i is also constant to within the accuracy of the measurements. For the sake of clarity in Fig.9, δ_i is displayed only for R_ℓ>6.7 A. The values of δ_e and

δ_i in the flat region are ~0.21 and ~0.12 respectively. As long as T>2.3K and R_ℓ>6.7 A, then, the "experimental" radii are related to the theoretical radius by a constant which is approximately equal to one. The significant point is that the proportionality constant is independent of both pressure and temperature in this region. Thus the pressure and temperature variation is accurately predicted by the Thomson equation using bulk values of n_ℓ and $\sigma_{\ell v}$. Furthermore, if we make the reasonable assumption that the departure of the constant from unity is only a measure of the imperfections of the scattering models, then we must conclude that in this "normal" region the Thomson equation is correct.

Consider now what may happen when R_ℓ decreases below 6.7 A. At this point the number of He atoms in the liquid drop is estimated to be ~25 by the Thomson equation. For a similar charged-drop system which contained this many atoms (or molecules) in it, macroscopic thermodynamics is still expected to be valid[7]. Hence the beginning of the change in δ at $R_\ell \cong$ 6.7 A in Fig.9 probably does not show the beginning of the failure of macroscopic thermodynamics due to the decrease in the drop size. Also we do not think that this increase arises from the imperfections of our scattering models since both δ_e and δ_i show the same qualitative dependence on the theoretical radius at R_ℓ>6.7 A. We believe that the deviation of the "relative difference" from

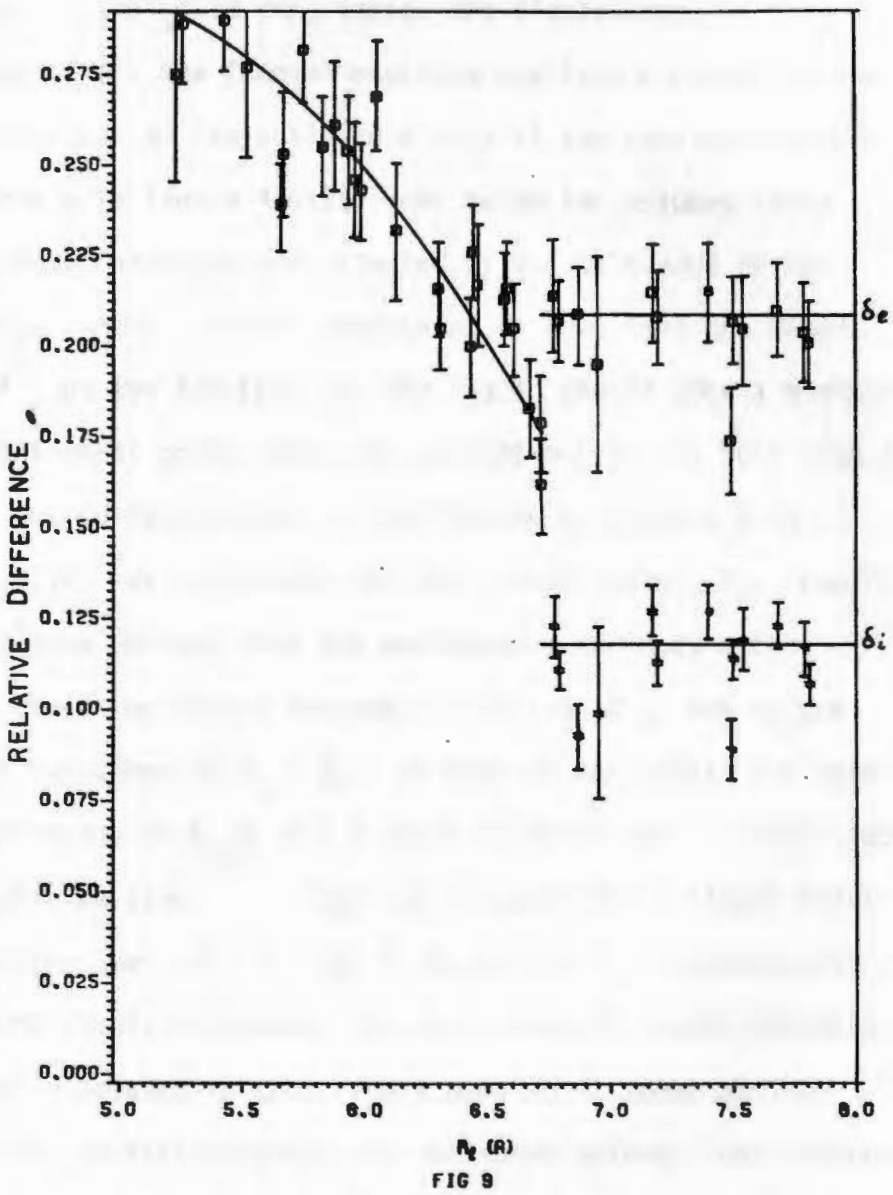

FIG 9

"Relative Differences", δ_e and δ_i, versus, theoretical radius R_I at T>2.3K. The solid lines through the data points are guides to the eye.

its constant value for small drop sizes is the effect of the existence of the solid core inside the liquid drop[28]. As mentioned before the Thomson equation predicts a change in the drop radius due to the solid core only if the surface tension and/or the bulk liquid density just below the assumed sharp liquid-vapor interface are effected by the existence of the solid core. Hence if this prediction is true then the dependence of δ on the thickness of the liquid should show a minimum liquid thickness below which the assumptions of the bulk liquid density and surfacetension in the Thomson equation are no longer valid. We calculated the solid core radius, R_s, from Eq.4 which is also derived from the macroscopic thermodynamics. $R_\ell - R_s$ gives the liquid thickness. In Fig.10 δ_e and δ_i are shown as functions of $R_\ell - R_s$. In both of the models δ's show a discontinuity at $R_\ell - R_s = 2.5$ A which is about equal to the size of a single He atom[29]. They are constant for a liquid thickness greater than $\sim$2.5 A. For $R_\ell - R_s < 2.5$ A, δ_e increases with decreasing liquid thickness. In this range of liquid thickness δ_i is not displayed in this figure because it shows similar temperature variations which are mentioned before. Our interpretation of this behavior is that the Thomson equation with bulk parameters works as long as the liquid layer is thicker than about a monolayer. Below this thickness the thermodynamic formalism is probably still valid, but the surface is becoming sufficiently influenced by the core structure so that the use of

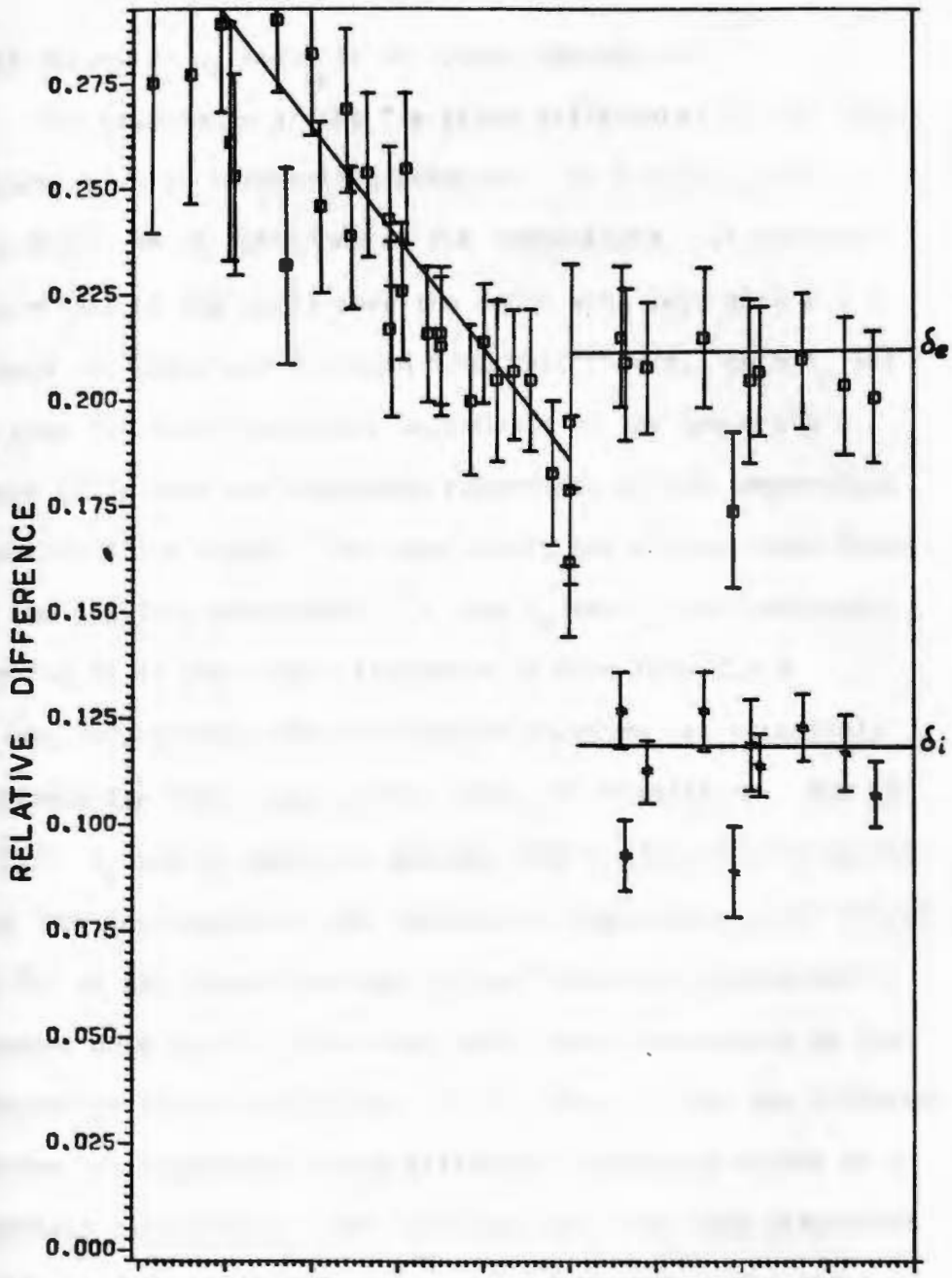

FIG 10

"Relative Differences", δ_e and δ_i, versus liquid thickness, $R_l - R_s$, at T>2.3K. The solid lines through the data points are guides to the eye.

bulk values of n_ℓ and $\sigma_{\ell v}$ is no longer appropriate[30].

The dependence of the "relative difference" on the temperature shows an interesting behavior. In Fig.11 δ_e and δ_i are displayed as functions of the temperature. To seperate the effect of the solid core the drops with less than 2.5 A liquid thickness are excluded from this figure. Both δ_e and δ_i show the same functional dependence on the temperature: Above ∿2.3K both are constants regardless of the temperature and saturation ratio. The same result has already been found in the previous paragraph; i.e. the δ_e and δ_i are constants for T>2.3K if the liquid thickness is more than 2.5 A . It was interpreted that the Thomson equation can accurately estimate the drop size in this range of temperature. But at T=2.3K, δ_e and δ_i start to deviate from their constant values and they increase with the decreasing temperature until T=1.9K. At T=1.9K the rate of change of the "relative differences" changes once again. Also they both show a dependence on the saturation ratio for T<2.3K, i.e. in Fig.11 δ has two different values corresponding to two different saturation ratios at a constant temperature. The splitting of δ for each saturation ratio starts at T=2.3K and increases with decreasing temperatures down to ∿1.9K. Below this temperature the splitting remains almost constant. For higher values of p/p_{sat} the deviation of δ from its constant value is more.

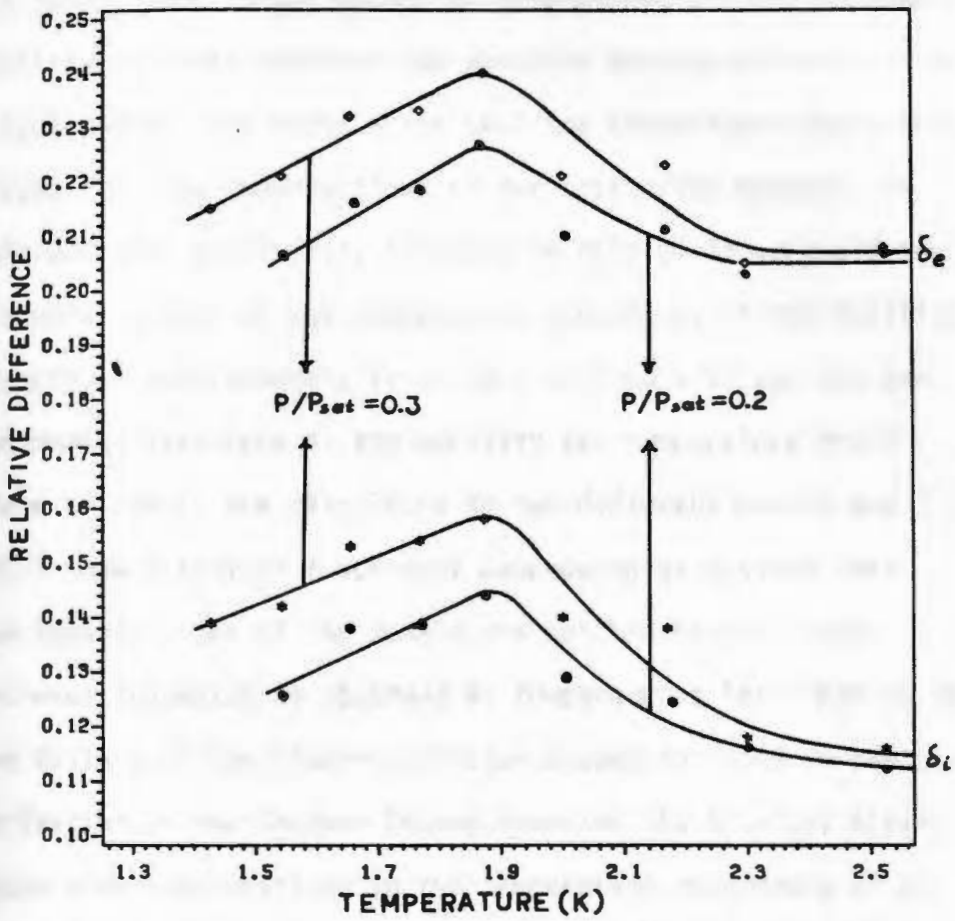

Fig. 11

"Relative Differences", δ_e and δ_i , versus temperature.
The solid lines through the data points are guides to the eye.

To be sure that the apparent temperature dependence of the "relative difference" reflects a physical reality, and is not an artifact of our method of determining δ from the measured mobility, we must consider the possible sources or error in our calculations. One might think that the temperature dependence arises from the imperfections in our scattering models. To rule out this possibility it would be helpful if we could see a similar effect on the temperature dependence of the mobility directly. Unfortunately it is very difficult to see any corresponding structure in the mobility vs. temperature graph since δ_e and δ_i are calculated in two different models and still show a similar functional dependence we believe that the imperfections of the models are not the cause of the increase in δ which is observed at temperatures less than $\sim$2.3K. The failure of the binary collision assumption used in the derivation of the Chapman Enskog equation (Eq.5) might also cause some complications in the temperature dependence of δ, since this equation is used to determine the experimental cross section, $\Omega^{(1,1)}_{exp}$, from the measured mobility. Fig.5 shows the estimated "boundary" between the binary and multiple collisions. It is clear that this "boundary" does not pass through a constant temperature and definitly not through 1.9K or 2.3K. Furthermore, as mentioned before, most of our data is in the binary collision regime. Hence this possibility

is also ruled out in explaining the temperature dependence of δ. As a result we conclude that even though our method of determining δ_e and δ_i is indirect and probably imperfect, the results displayed in Figures 11 and 12 have physical significance.

Before we draw any conclusion from the temperature dependence of δ, it might be helpful to see the variation of the "relative difference" with the liquid thickness at low temperatures. In Fig.12 δ_e and δ_i are displayed as functions of $R_\ell - R_s$ for T>2.3K (see Fig.10) are also drawn for comparison. The δ's for intermediate temperatures (1.9K <T<2.3K) are not shown in this figure for the sake of clarity. But reasonably enough they lie in between the solid and the dashed lines. At a given liquid thickness the difference between the solid and the dashed lines shows the deviations of δ_e and δ_i from their constant values for which the Thomson equation is found to be valid. Fig.12 shows that the deviation starts as soon as the liquid thickness becomes more than a monolayer ($\sim$2.2 A), and it increases with the increasing thickness of the liquid helium. Because of the lack of data for $R_\ell - R_s$<2.5 A at low temperatures, the effect of the solid core can not be seen in this figure. But the effect is observed for some intermediate temperatures. No difference is found between the high and the low temperature δ's for $R_\ell - R_s$<2.5 A. Since the ion-solid-liquid complex is almost completely solid for this range of the liquid thickness,

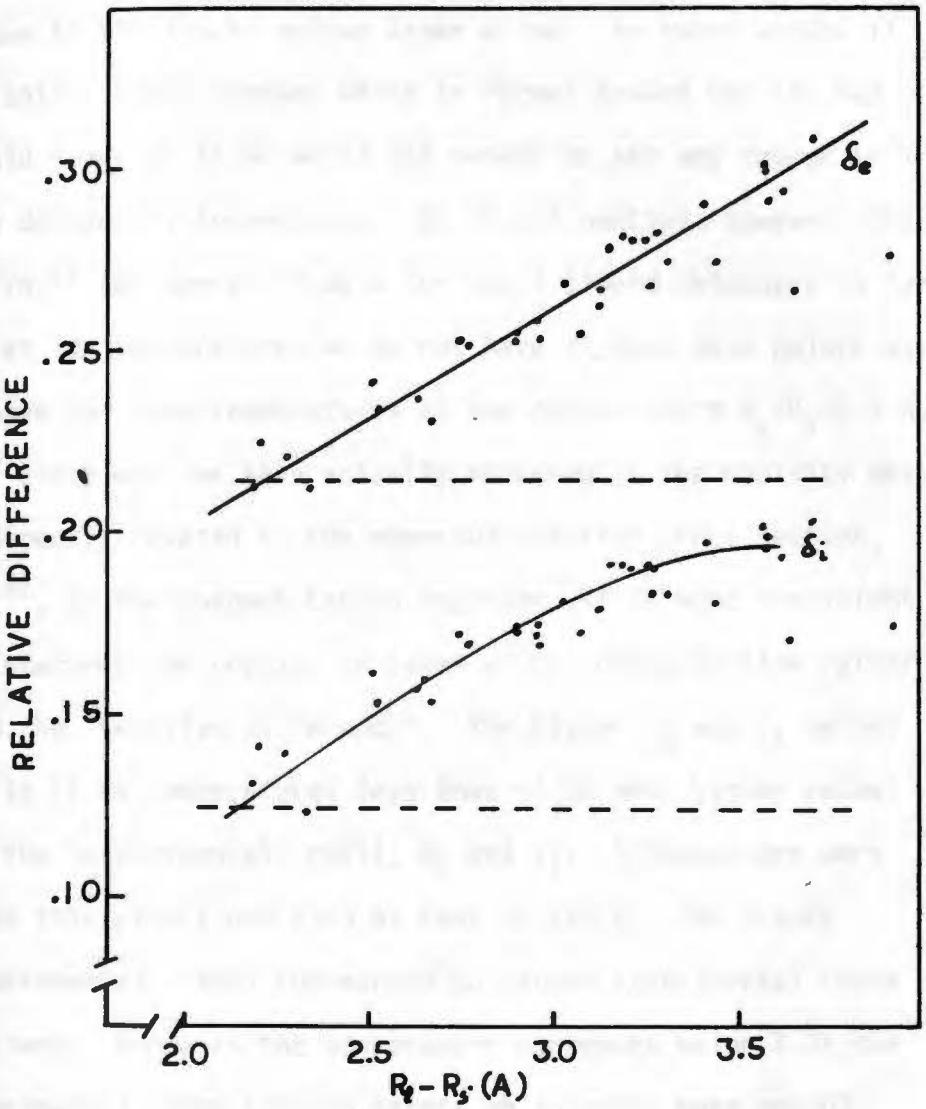

Fig. 12

"Relative Differences", δ_e and δ_i, versus liquid thickness R_1-R_s, for T 1.9K. The dashed lines show the same relation for T 2.3K. The solid lines through the data points are guides to the eye.

above result suggests that the change in δ, starting at T=2.3K is due to the liquid helium layer alone. In other words, if the solid-liquid complex which is formed around the ion has no liquid layer on it we would not expect to see any change in δ with decreasing temperature. We should mention, however, that in Fig.12 the spread of data for small liquid thickness is large, and at low temperatures we do not have as many data points as we have for high temperatures at the region where $R_\ell - R_s < 2.5$ A.

Since what we have actually measured is the mobility which is directly related to the momentum transfer cross section, $\Omega^{(1,1)}$, by the Chapman Enskog equation, it is more convinient to interpret the results in terms of the cross section rather than the "relative difference". The higher δ_e and δ_i values in Fig.11 at temperatures less than $\sim$2.3K mean higher values for the "experimental" radii, R_e and R_i. Although not very clear this effect can also be seen in Fig.8. The bigger "experimental" radii correspond to larger experimental cross sections. Hence as the temperature decreases below 2.3K the experimental cross section starts to increase more rapidly than expected in the model. A rapid increase in the experimental cross section means either an increase in the actual (not "experimental") drop size which is not predicted by the Thomson equation, or it might also mean a change in the nature of collisions, without an actual increase in the drop size. The calculations of the cross ections in different models show that

for a given temperature and drop radius the "inelastic" model gives larger cross sections than the elastic model. Hence large cross sections at low temperatures imply that collisions start being more inelastic at ∿2.3K. It is also possible however that the nature of the interaction changes as temperature decreases below 2.3K. Unfortunately it is impossible to draw any reliable conclusions with the present information. Nonetheless, any change in the nature of the scattering with the temperature in a rather peculiar way still needs an explanation. One might think that the number of atoms on the surface of the drop changes with the temperature, and changing surface occupancy might cause a change in the nature of the scattering. But this is hardly the case since the same effect is not observed at high temperatures. Another possible cause of such behavior might be a superfluid transition that liquid helium layer undergoes at ∿1.9K, and which is broadened up to ∿2.3K. Although it is difficult to believe that there is a λ-point transition starting from the second atomic layer of liquid helium, it does explain the general features of our results. The suppression and the broadening of the bulk transition temperature (2.17K) for finite systems is known (20). Qualitatively, ∿1.9K for transition temperature and ∿0.4K broadening above the transition temperature is consistent with this fact.

One needs to have more information to be able to explain the details of the variation of the cross section with the temperature. But it is not unreasonable to expect a change in the scattering process as the liquid layer passes through a transition from the normal fluid to superfluid as the temperature decreases. This change might favor an increase in the cross section at low temperatures. For example we can speculate that during a collision, the proposed superfluid helium layer will deform under the influence of the attractive van der Waals field of an incident atom because of the lack of friction between the solid core and the liquid layer. Under this condition the drop will appear bigger to the incident atom. This will result in a larger momentum transfer cross section. As mentioned before, the difference between δ's at high and low temperatures does not exist if the liquid layer becomes less than a monolayer. Existence of a superfluid transition can also explain this observation: Since in this range of the liquid thickness the ion-solid-liquid complex becomes almost completely solid, no superfluid transition and hence no difference between δ's at the high and the low temperatures should be expected.

We feel that with the present data any further comment on the temperature dependence of the momentum transfer cross section, $\Omega^{(1,1)}$, can not be more than a speculation. Perhaps more information is needed to give a satisfactory explanation of this point.

To summarize our results: First, we have shown the existence of the drop formation around the $^{+}$He ions, directly from the mobility measurements. This is a qualitative verification of the Thomson equation. Secondly, by comparing the model dependent "experimental" radii with the Thomson equation predictions we have concluded that macroscopic thermodynamic arguments can explain in detail the sizes of the microscopic helium drops with radii between 6.7 A - 9 A. The comparison also showed that there is a solid core within the liquid drop and its radius can also be determined by the thermodynamical arguments. No effect of the solid core on the liquid drop radius is found untill the liquid thickness becomes less than 2.5 A at which the solid core changes the properties of the liquid-vapor interface. This result is also in complete agreement with the Thomson equation. Finally, we have found an unexpected increase in δ_e and δ_i (or in the experimental cross section) as the temperature decreases. The increase starts at $\sim$2.3K and reaches its maximum value at $\sim$1.9K. This result is interpreted as, with decreasing temperature, either an increase in the actual drop size which is not predicted by the Thomson equation, or a change in the nature of the collisions which keeps the drop size unchanged. Although the present data is not enough to make a completely satisfactory explanation, we suggested that the dependence of the experimental cross section might be an indication of a superfluid transition in the liquid

helium layer of the ion-solid-liquid complex. According to our results the transition temperature is ∿1.9K and it is broadened up to ∿2.3K. The suggested transition starts when the thickness of the liquid layer becomes more than a monolayer.

REFERENCES

1. M.Volmer and A.Weber, Z.Physik.Chem, Leipzig 119, 277 (1926).
2. J.Frenkel, Kinetic Theory of Liquids, (Oxford University Press, Oxford, England, 1946), p.394.
3. K.C.Russell, J.Chem.Phys. 50, 1809 (1969).
4. K.R.Atkins, Phy.Rev. 116, 6, 1339 (1959).
5. K.W.Schwarz, Adv.Chem.Phys. 33, 1 (1974).
6. J.J.Thomson, Application of Dynamics to Physics and Chemistry, (MacMillan, London, 1888).
7. A.W.Castleman Jr., M.Holland and G.Keesee, J.Chem.Phys. 68, 4 (1978).
8. I.Džidić and P.Kebarle, J.Phys.Chem. 74, 1466 (1970).
9. J.L.Katz and B.J.Ostermier, J.Chem.Phys. 47, 478 (1967).
10. J.L.Katz, C.J.Scoppa II, N.G.Kumar and P.Mirabel, J.Chem.Phys. 62, 448 (1975).
11. J.A.Northby and G.Akinci, "Ion Droplet Mobility in Cryogenic ^{4}He Vapor" J.Phys. 39, Colloq. C6, 84-85 (1978).
12. J.A.Northby and G.Akinci, "Charged Droplets in Cryogenic ^{4}He vapor" Phys.Rev.Lett. 42, 573-576 (1979).
13. J.A.Northby, G.Akinci and L.S.Lagurney, "Positive Ions in Cryogenic ^{4}He Vapor" in Proc. of 12th Symp. on Rarefied Gas Dynamics, 1145 (1981).
14. G.Akinci and J.A.Northby, Proc. of 16th Int.Conf. on Low Temp. Phys., 575 (1982).

15. A.Dahm and T.M.Sanders Jr., J.Low Temp.Phys., 2, 199 (1970).

16. B.L.Henson, Phys.Rev. A 15, 1680 (1977).

17. K.W.Schwarz, Phys.Rev. A 6, 837 (1972).

18. H. van Dijk and M.Durieux, Physica XXIV, 920 (1958).

19. J.R.Eckardt et al., Phys.Rev. B 16, 1944 (1977).

20. J.Wilks, The Properties of Liquid and Solid Helium (Clarendon Press, Oxford, 1967).

21. J.K.Smith et al., Phys.Rev. A 13, 1422 (1976).

22. D.O.Edwards and W.F.Saam, Prog. Low Temp.Phys. Vol VII A, Ch.4 (ed. by D.F.Brewer, North-Holland Publishing Company,1978).

23. $\sigma_{s\ell}$ = 0.1 dyne/cm is found by using the surface tension of solid-liquid interface as an adjustable parameter to fit the mobility and viscosity data of $^{+}$He ions in liquid helium to the Atkins model. See reference 5.

24. E.W.Daniel and E.A.Mason, The Mobility and Diffusion of Ions in Gases Ch.5 (John Wiley and Sons, New York, 1973).

25. P.S.Epstein, Phys.Rev. 23, 710 (1924).

26. L.W.Bruch and I.J.McGee, J.Chem.Phys. 52, 5884 (1970).

27. T.G.Wang et al., Phys.Rev.Lett. 30, 485 (1973).

28. The existance of a solid core formed around He ions in bulk liquid helium has already been observed. See references 4 and 5.

29. The "diameter" of a single He atom is 2.2A. See reference 20.

30. It should be mentioned that the maximum value of $R_\ell - R_s$ is only $\sim$3.3A which is less than two atomic layers of helium.

APPENDIX A

The Thomson Equation

In this research we have used the Thomson equation as the theoretical base to compare our experimental results. By this comparison we have checked the validity of the macroscopic thermodynamics when it is applied to the microscopic systems and we also obtained information about the structure of the microscopic helium drops. Since the Thomson equation has played a central role in the interpretation of the experimental results its derivation from the thermodynamical arguments will be given in this appendix. To be able to show clearly that the drop radius which is given by the Thomson equation is not effected by the existence of a solid core we will assume a solid core in the liquid drop.

When an ion is placed in a polarizable vapor, the vapor atoms will be polarized in the electric field of the ion. Hence an attractive polarization force will be created between the ion and the neutral vapor atoms. The effect of the polarization potential will be an increase in the Gibb's free energy of the system. To reduce the free energy, or equivalently, to reduce the effect of the ion, a liquid drop will form around the ion. Above reasoning is valid also for an ion in

a liquid. Therefore it is reasonable to expect a solid core within the liquid drop. But in the absence of the ion the liquification and the condensation are not favorable at pressures less than the saturated vapor pressure because the free energies of the liquid and the solid phases are more than the free energy of the gas phase at $p<p_{sat}$. Hence the total change, ΔG, in the free energy, G, of the system due to the formation of the solid-liquid complex around the ion can be written as;

$$\Delta G = \Delta G_e + \Delta G_s + \Delta G_\ell \qquad (A-1)$$

where ΔG_e is the decrease in the free energy due to the reduction in the electric field energy, and, ΔG_s and ΔG_ℓ are the increases in G due to the condensation and the liquification respectively. At the thermal equilibrium ΔG is minimized.

ΔG_e is the difference between the electric field energies of an ion with charge e and radius R_o surrounded by the two concentric dielectric spheres of solid and liquid with radii r_s and r_ℓ, and of the same ion in a vapor. The energy density, u, in the presence of a dielectric is given by;

$$u = |\vec{D}|^2/8\pi\epsilon \qquad (A-2)$$

where $\vec{D}$ is the displacement vector with magnitude e/r^2 and ϵ is the dielectric constant. If the interactions between the polarized atoms are ignored $\epsilon=1+4\pi\alpha n$ where α is the atomic polarizability. ΔG_e can be expressed in terms of the energy

densities u_s, u_ℓ and u_v of the solid, the liquid and the vapor as;

$$\Delta G_e = \int_{R_o}^{r_s} u_s \, d\tau + \int_{r_s}^{r_\ell} u_\ell \, d\tau - \int_{R_o}^{r_\ell} u_v \, d\tau \qquad (A\text{-}3)$$

where $d\tau$ is the volume element. If we assume that the dielectric constant of the vapor is 1, and of the solid and the liquid nearly 1, then equation A -3, together with A -2, will give;

$$\Delta G_e = 2\pi\alpha e^2 [n_s(1/r_s - 1/R_o) + n_\ell(1/r_\ell - 1/r_s)] \qquad (A\text{-}4)$$

ΔG_ℓ and ΔG_s can be calculated from the thermodynamical arguments. In Fig. A -1 the free energies per atom, chemical potentials, of vapor, liquid and solid phases are shown schematically as functions of pressure. At a constant temperature;

$$d\mu = v \, dp \qquad (A\text{-}5)$$

where v is the atomic volume. If the liquid and the solid is assumed to be incompressible the chemical potentials of the liquid and the solid should change with pressure linearly as they do in this figure. The slopes of the lines ℓ and s are v_ℓ and v_s, the atomic volumes of the solid and the liquid respectively. $\Delta\mu_\ell$ and $\Delta\mu_s$ are the increases in the chemical potential due to the liquification and the condensation of an atom at pressure p. From the geometry of the figure;

$$\Delta\mu_\ell = \Delta\mu_1 - \Delta\mu_2 \qquad (A\text{-}6)$$

If the vapor is ideal and if $v_g >> v_\ell$, the equations A -5 and A -6 will give;

$$\Delta\mu_\ell = -kT \ln p/p_{sat} \qquad (A-7)$$

$N_\ell = n_\ell 4/3\pi(r_\ell^3 - r_s^3)$ is the number of atoms which condense to form a homogeneous liquid drop with a solid core in it. n_ℓ and r_ℓ are the density and the radius of the liquid drop and r_s is the radius of the solid core. Then;

$$\Delta G_\ell = -kTN_\ell \ln p/p_{sat} + \sigma_{\ell v} 4\pi r_\ell^2 \qquad (A-8)$$

where $\sigma_{\ell v}$ is the surface tension of the liquid-vapor interface. The second term on the right hand side of the Eq.A -8 is the surface energy which can not be neglected for small drops with large surface/volume ratio. Similarly for the solid core inside the liquid;

$$\Delta\mu_s = (\Delta\mu_\ell + \Delta\mu_3 + \Delta\mu_4) \qquad (A-9)$$

and

$$\Delta G_s = -kTN_s \ln p/p_{sat} + \sigma_{s\ell} 4\pi r_s^2 \qquad (A-10)$$

where $\sigma_{s\ell}$ is the surface tension of the solid-liquid interface and $N_s = n_s 4/3\pi r_s^2$. In Eq.A -10 an incompressible solid with density $n_s >> n_g$ is assumed.

The total free energy change, ΔG, is the summation of the Equations A -4, A -8 and A -10. At thermal equilibrium both $\partial\Delta G/\partial r_\ell$ and $\partial\Delta G/\partial r_s$ must be zero. The first of these conditions gives the Thomson equation with the drop radius R_ℓ;

$$kT\ln(p/p_{sat}) = 2\sigma_{v\ell}/n_\ell R_\ell - \alpha e^2/2R_\ell^4 \qquad (A\text{-}11)$$

The second condition of the thermal equilibrium gives Eq. 5 of the manuscript if $p \ll p_m$ is satisfied.

$$kT\ln(p/p_{sat}) - p_m/n_s = 2\sigma_{s\ell}/(n_s - n_\ell)R_s - \alpha e^2/2R_s^4 \qquad (A\text{-}12)$$

where R_s is the solid core radius at thermal equilibrium.

Above derivation shows how the macroscopic thermodynamics enter the derivation of the Thomson equation; and it also shows that the drop radius which is predicted by the Thomson equation is not effected by the presence of the solid core inside the drop. The drop radius only depends on the surface tension, $\sigma_{\ell v}$, and the assumed bulk liquid density, n_ℓ, just inside the sharp liquid-vapor interface.

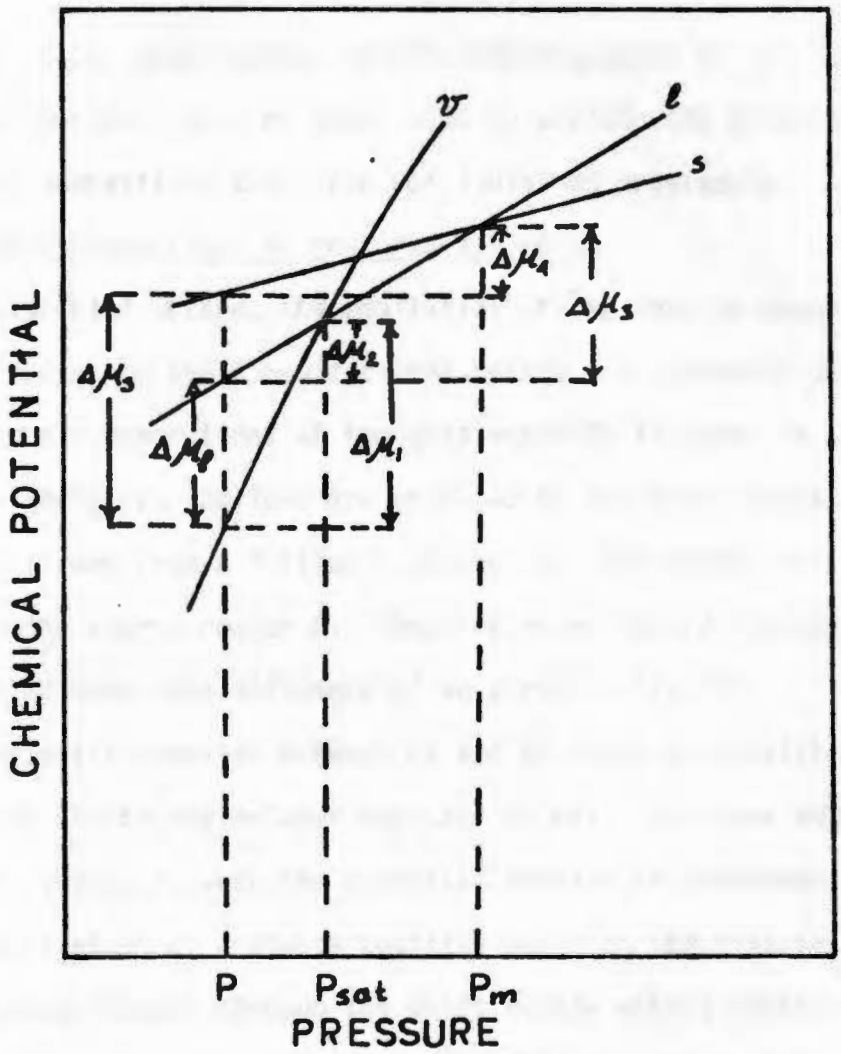

Fig. A1

The pressure dependence of the chemical potential of vapor, liquid and solid phases. The different terms are explained in the text.

APPENDIX B

EXPERIMENTAL DETAILS

Most of the experimental details are discussed in section II of the manuscript. Here we would like to explain the electronic and vacuum connections that were not explained previously.

1.Electronic connections of the Grid Assembly

As discussed before, the mobilities of $^{+}$He ions He vapor are measured by pulsed-time-of-flight method. A schematic of the electronic connections of the grid assembly is shown in Fig. B-1. Briefly, $^{+}$He ions are produced by the bombardment of the electrons from a tritium β source, S. The drops are formed in the source region A. They are moved toward the gate region G1-G2 under the influence of an electric field E_s. A small potential barrier between G1 and G2 keeps the positive ions in the source region when the gate is off. The ions enter the drift region, B, when the potential barrier is overcomed by the application of a square positive pulse on the grid G1. The ion pulses travel through the drift region with a constant drift velocity, v_d, in a uniform drift field E_d. Ion pulses create an induced current on the collector C as they pass through the grid G3. The current pulse is first amplified and then signal averaged to eliminate the noise. The travel time of $^{+}$He ion pulses from G2 to C is measured.

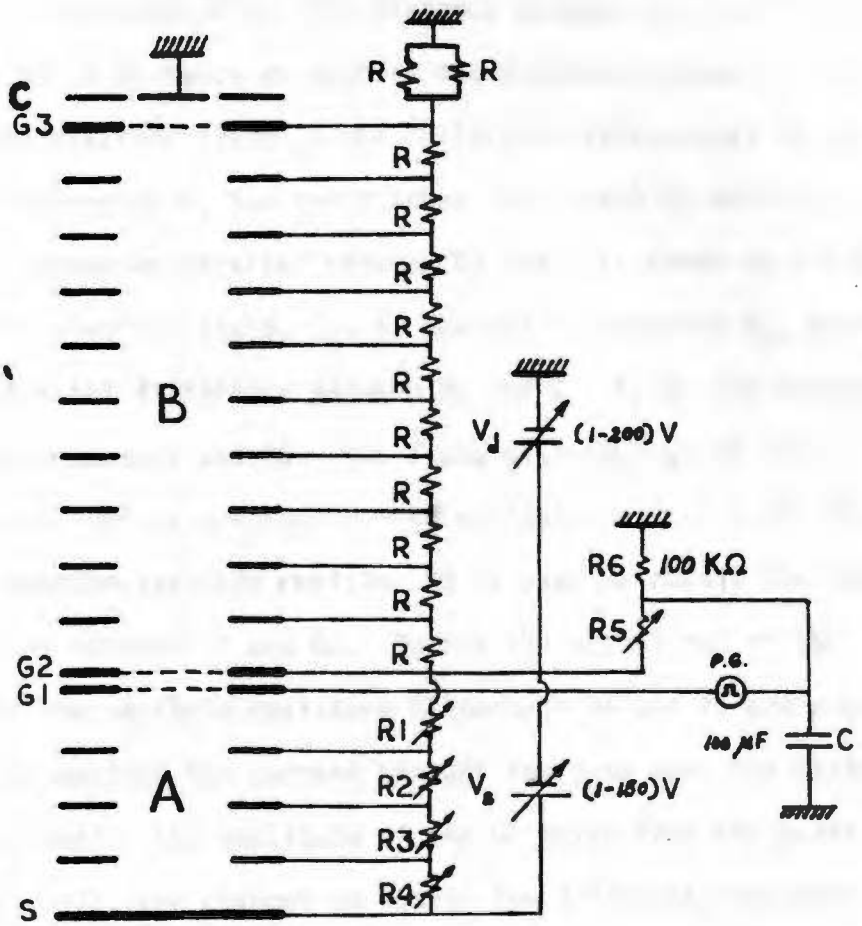

Fig. B1

The schematic of the electronic connections of the grid assembly.

To obtain a uniform field in the drift region, the equally spaced electrodes between G2 and G3 are seperated by 10KΩ precission resistors, R's. The distance between the electrodes is 1.00cm which is twice as much as the distance between G3 and C. To make the electric field in the collector region equal to the field in the region B, two resistances, R's, each of which is 10KΩ, are connected parallel between G3 and C as shown in Fig.B-1. The uniform electric field, E_d, is changed by changing V_d, which is the potential difference between G2 and C. V_s is the potential difference between S and G2. The field distribution in the source region can be arranged by the variable resistors R1, R2, R3 and R4. Another variable resistor R5 is used to change the potential barrier between G1 and G2. During the actual run of the experiment the variable resistors R1 through R4 and R5 are preset to give the maximum ion current through the gate when the pulse is on. V_s and/or the amplitude of the G1 pulse from the pulse generator, P.G., are changed to obtain the different ion pulse amplitudes.

2. Electronic connections for the time of flight measurements

The schematic of the electronic connections to measure the time of flight of the ion pulses is shown in Fig.B-2. A pulse generator, P.G.I, connected to a function generator, F.G., is used to create a positive square pulse (G1-pulse) to cause the $^{+}$He ions enter into the drift region. The current pulses, the

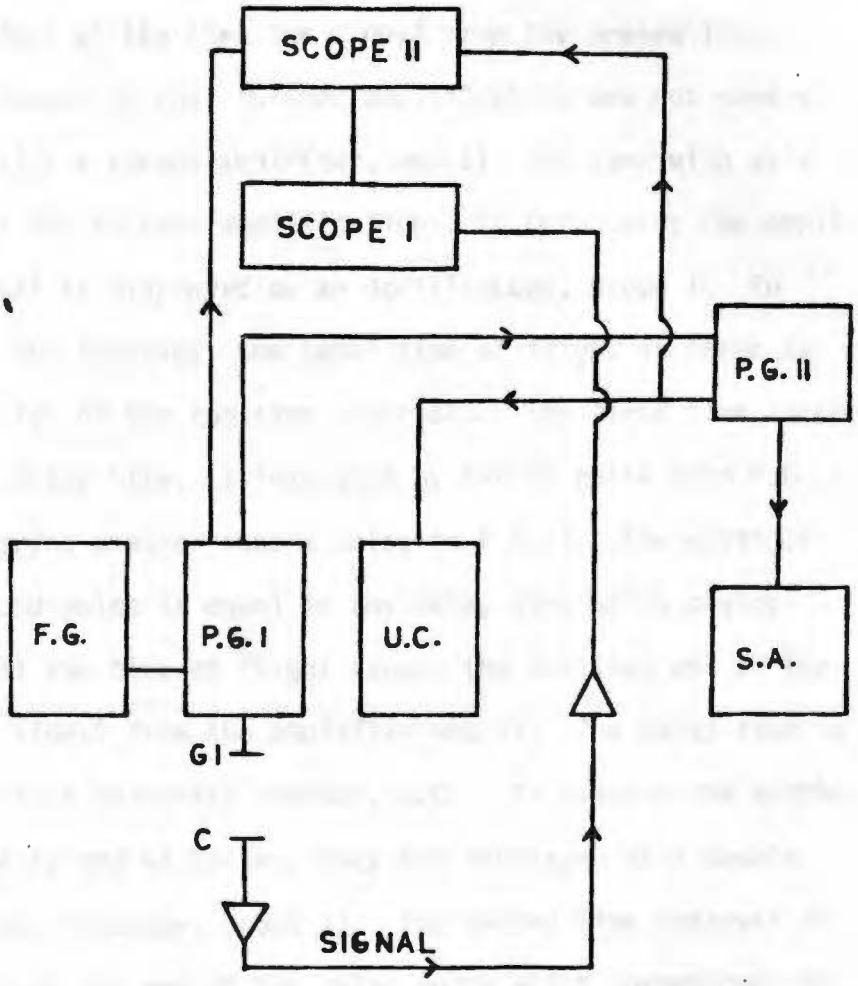

Fig. B2

The electronic connections for the time of flight measurements.

SIGNAL, created by the arrival of the $^{+}$He ions to the collector, C, are first amplified by the preamplifier which is an Analog Device 41J operational amplifier used with $10^{9}\Omega$ feedback resistance. Most of the time the signal from the preamplifier was big enough so that further amplification was not needed. Occasionally a second amplifier, amp.II, was used with gain at most 5 for further amplification. In both cases the amplified signal is displayed on an oscilloscope, Scope I. To increase the accuracy, the total time of flight is taken as the addition of the two time intervals. The first time interval, the delay time, is initiated by the G1 pulse from P.G. I by triggering another square pulse in P.G.II. The width of this second pulse is equal to the delay time which covers almost all the time of flight except the trailing end of the original signal from the amplifier amp.II. The delay time is measured by a universal counter, U.C.. To compare the widths of the delay and G1 pulses, they are displayed on a double channel oscilloscope, Scope II. The second time interval is initiated by the end of the delay pulse which corresponds to the trailing end of the amplifier signal. Only this portion of the signal is averaged by a Fabri-Tek 1010 digital signal averager to be able to make accurate measurement of the time of flight. The two time intervals are shown schematically in Fig.B-3. The total time of flight, τ_d, is equal to $t_1 + t_2$.

The details of the determination of the second time interval t_2 is given in the manuscript.

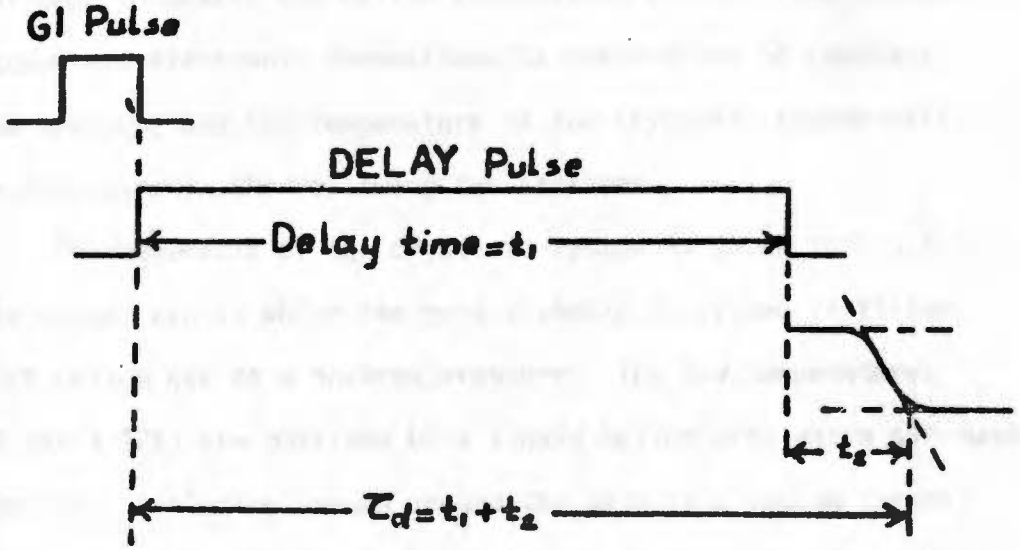

Fig. B3

The two time intervals, t_1 and t_2.

3. Cryogenic system

The temperature range of this system is 1.32K-4.22K. To obtain and maintain such low temperatures require a special technique. Part of the details of this technique is discussed in the manuscript. In this section we will give a diagram of the cryogenic system and explain the procedure that we have followed to obtain the helium temperature (4.2K). The necessary vacuum and electronic connections to measure and to regulate the pressure and the temperature in the cryogenic system will be discussed in the following two sections.

The schematic of the cryogenic system is shown in Fig.B-4. The copper can in which the grid assembly is placed is filled with helium gas at a desired pressure. The low temperatures (1.32K-4.22K) are obtained by a liquid helium bath which surrounds the can. Isolation vacuum around the bath is a vacuum jacket which thermally isolates the liquid helium bath from the surroundings. Finally the liquid helium dewar is placed in a liquid nitrogen bath at 77K.

Before each run of the experiment the system is cooled down to 4.2K, the boiling temperature of helium at atmospheric pressure, by the following procedure: First, the can, the bath and the isolation vacuum are evacuated to assure the cleanliness. $\sim 1 \times 10^{-4}$ torr pressure is achieved in the can and in the isolation vacuum at this stage. Then the isolation vacuum is filled by the nitrogen gas from the liquid nitrogen boil off up to 1-2 torr to make the

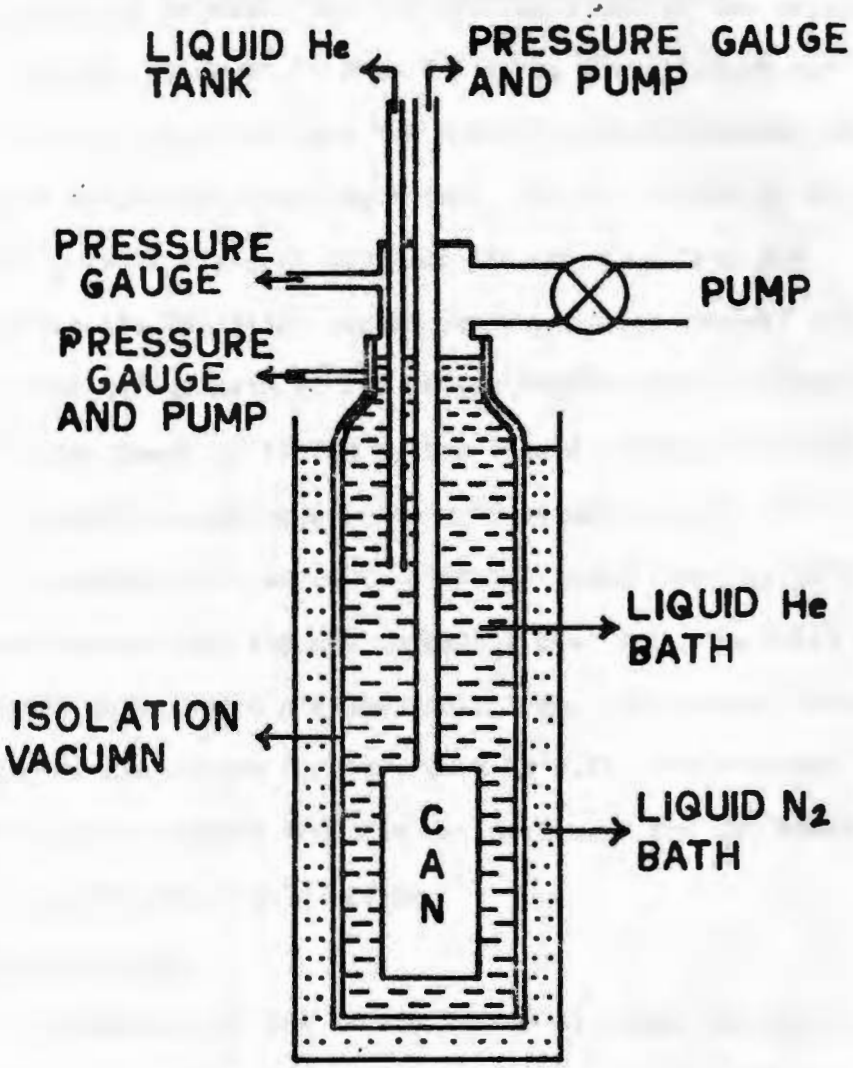

Fig. B4

The cryogenic system.

thermal contact between the nitrogen and helium dewars. Later when the system is at helium temperatures the exchange gas, nitrogen, freezes and the vacuum is achieved in the isolation vacuum again to maintain the thermal isolation of the helium bath. The helium dewar is also filled by the nitrogen gas up to 1 At. pressure to make the thermal contact between the isolation vacuum and the copper can. He gas can not be used for this purpose since it diffuses through the glass and enters into the isolation vacuum causing a poor thermal isolation of the helium bath at the helium temperatures. Finally, the nitrogen dewar is filled by the liquid nitrogen to cool down the whole system except the grid assembly up to 77K. The grid assembly is cooled to nitrogen temperature by letting pure helium gas into the can through a charcoal trap which is surrounded by a liquid nitrogen cold trap. To reduce the temperature of the system further, down to 4.2K, the nitrogen exchange gas is pumped from the helium dewar, and the dewar is filled with the liquid helium.

4. Vacuum system

The schematic of the vacuum system is shown in Fig.B-5. The cryogenic system is viewed from the top in this figure. The can and the bath pressures are measured by the capacitance manometer, MKS Baratron Model 170, through the valves 2 and 1 respectively. This pressure gauge measures the differential pressure, i.e. the pressure measured with respect to a reference pressure. The reference pressure is obtained by pumping the volume between

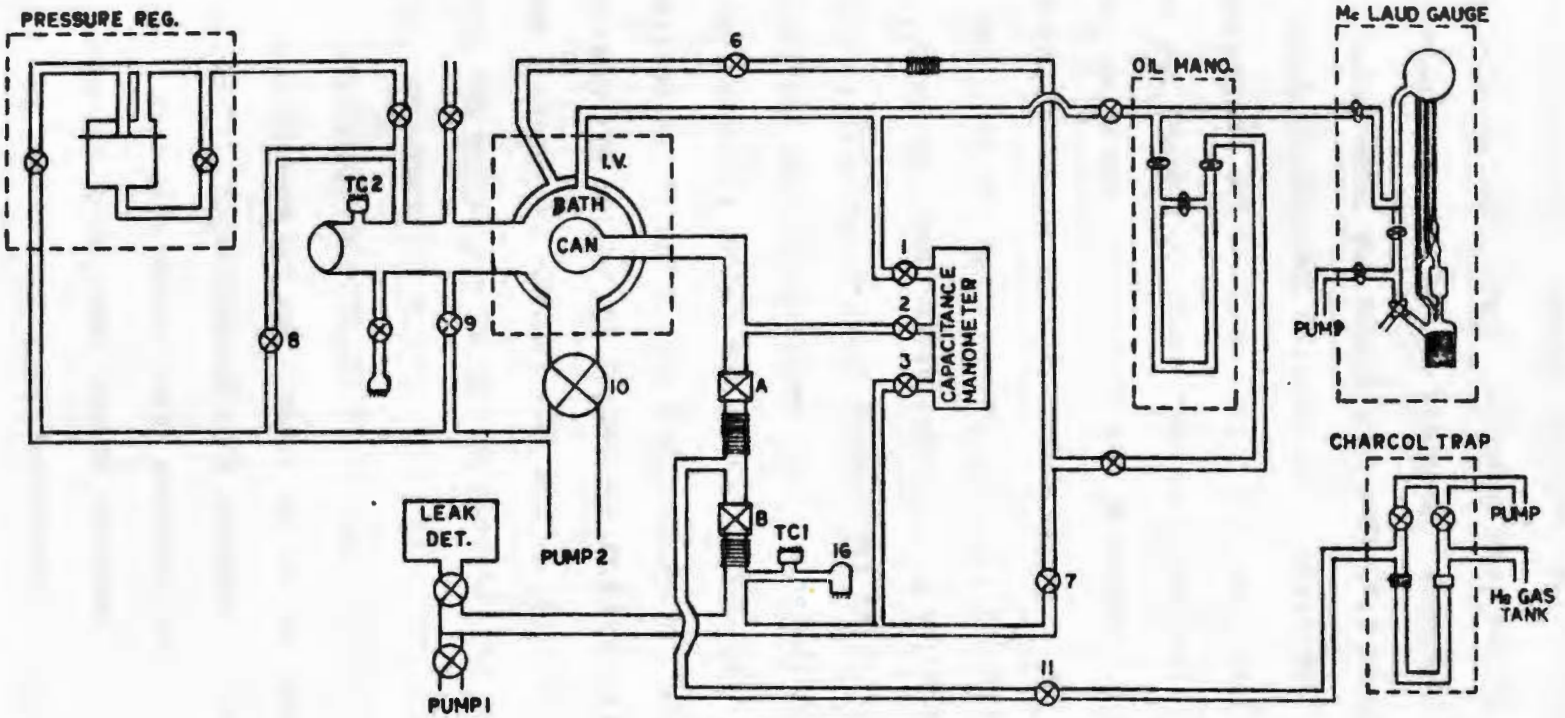

Fig. B5

The vacuum system.

the values B,3 and 7 by a mechanical pump, PUMP 1, and the relative value of it is measured by the capacitance manometer through the valve 3. The absolute value of the reference pressure (~20 mtorr) is measured by a thermocouple, TC1, which is calibrated against the McLaud gauge. The oil manometer is used to check the linearity of the capacitance manometer between the pressures 5 torr - 40 torr. During the experiment the pressure in the can is increased by letting the helium gas from the liquid helium boil off in the bath through the valves 1 and 2. Can pressure is decreased by pumping the helium gas from the can by PUMP1 through the valves A and B or 2 and 3. As mentioned in the manuscript, the temperature of the system is determined from the bath vapor pressure. The coarse temperature regulation is obtained by controling the pumping speed on the bath by valves 10, 9 and a needle valve 8. At temperatures above the superfluid transition temperature 2.17K, the thermal conductivity of the liquid helium is low [20]. The evaporation at relatively hot spots in the liquid helium creates wrinkles on the surface which results in oscillations in the bath pressure. Hence to control the temperature is more difficult if T>2.17K. Between the temperatures 2.17K - 3.0K, in a addition to controlling the pumping speed, a pressure regulator is also used to regulate the temperature. Before each run of the experiment, the whole vacuum system is evacuated and leak checked by the leak detector. Cleanliness is most important in the can and in the isolation vacuum. Therefore these two parts of the vacuum system are pumped by PUMP1 and a diffu-

sion pump which is placed in the leak detector through valves A and B and 6, 7 for two or three days to achieve a pressure of $\sim 1 \times 10^{-4}$ torr. This pressure is measured by the ion gauge, IG. As mentioned in the previous section, to cool down the grid assembly, pure helium gas is let into the can through the charcoal trap and the valves 11 and A.

The vacuum system is mounted on a table which sits on vibration absorbers.

5.Temperature control system

The fine temperature regulation of the experimental cell is obtained by an uncalibrated Ge resistor in a bridge circuit and is used with a heator in a feedback circuit. The bridge circuit and the electronic connections of the temperature control system are shown schematically in Figures B-6 and B-7 respectively. The locations of the various components of the bridge circuit are indicated in Fig B-6. The 35Hz ac voltage is supplied by the Lock-in amplifier Ref→Bridge amplifier Ref Derive as shown in Fig.B-7. The Ge resistor, R_{Ge}, is placed in the liquid helium dewar, on top of the can. The resistance of the Ge resistor is sensitive to the temperature changes in the dewar at helium temperatures. A slight temperature change in the dewar is enough to cause a difference between R_{Ge} and R_B which are shown in Fig.B-6. As a result a current passes through the detector. This current signal is amplified by the bridge amplifier first. The output signal, SIG, can be observed on the oscilloscope. The signal is then sent to the lock-in amplifier for further

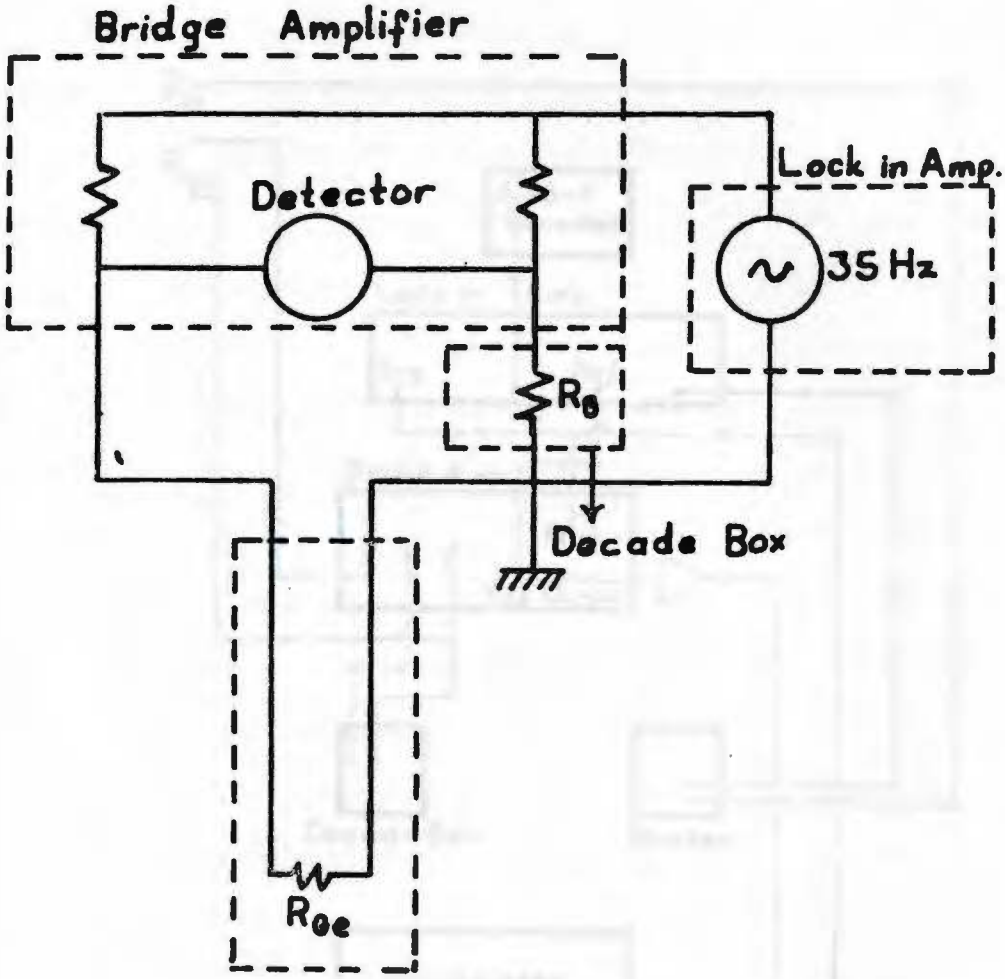

Fig. B6
The bridge circuit.

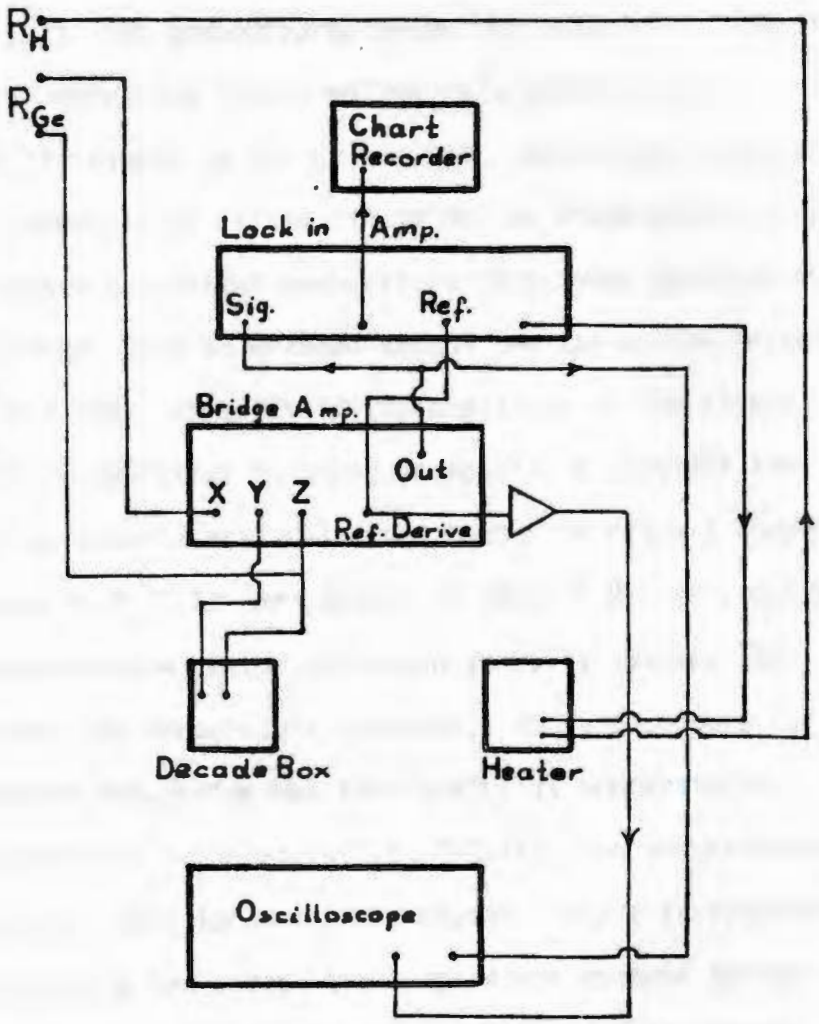

Fig. B7

The electronic connections of the temperature control system.

amplification. The final signal which corresponds to the temperature deviations in the dewar is observed on the chart recorder. To regulate the temperature a 100Ωresistor, R_H, is used in a feedback circuit. At temperatures below the superfluid transition temperature at which the liquid helium is a perfect thermal conductor, R_H is placed on top of the can. Above this temperature, the thermal conductivity of the liquid helium drops drastically . Hence to maintain a constant temperature throughout the experimental cell a chromel wire is wrapped around the can as the heator resistor at T>2.17K. Normally if the amplitude of the signal from the lock-in amplifier is zero, indicating a constant temperature in the experimental cell, the heator in Fig.B-7 supplies ∿2V dc voltage to R_H. It corresponds to ∿4×10^{-2} W. If a nonzero signal is received the heator unit automatically changes this voltage to keep the temperature constant. Above procedure for fine temperature regulation was very useful at temperatures below the superfluid temperature. At T>2.17K, the temperature fluctuations were very large for the heator circuit to regulate. Therefore, except a few cases, the temperature control system is only used to record the relative temperature on the chart recorder.

APPENDIX C

CALCULATIONS OF MOMENTUM CROSS SECTIONS

To be able to calculate the momentum cross section, $\Omega^{(1,1)}$, the interaction potential between the charged drop and the neutral vapor atom must be known. We assumed that this potential is the addition of polarization potential, $-c/r^4$, and the summation of all the van der Waals interactions, $-c_6/r^6+c_{12}/r^{12}$, between the vapor atom and each of the neutral liquid atoms. If the drop is assumed to have constant density the total of van der Waals interactions can be calculated by replacing the summation with an integration over the volume of the drop. The resultant potential is;

$$V(r)=-c/r^4-Ac_6\frac{R^3}{(r^2-R^2)^3}+\frac{Ac_{12}}{15}\frac{R^3(15r^6+63R^2r^4+45R^4r^2+5R^6)}{(r^2-R^2)^9} \qquad (C\text{-}1)$$

where $A=4\pi n_\ell/3$, n_ℓ is the number density of the liquid, $C=\alpha e^2/2$, α is the atomic polarizability, and R is the radius of the drop. In above equation first term represents the polarization interactions, second and third terms are the total of repulsive and attractive parts of van der Waals interactions respectively.

Above potential can be written in terms of reduced variables as;

$$V^*(r^*)=-\frac{P^*}{R^{*4}}\frac{1}{r^{*4}}-\frac{f(R^*,P^*)}{R^{*6}}\frac{1}{(r^{*2}-1)^3}+\frac{g(R^*,P^*)}{R^{*12}}\frac{15r^{*6}+63r^{*4}+45r^{*2}+5}{(r^{*2}-1)^9} \qquad (C\text{-}2)$$

where

$$f(R^*,P^*)=\frac{(1-R^{*2})^3}{5R^{*2}-117R^{*4}-99R^{*2}-15}\left[-6(27R^{*4}+27R^{*2}+5)+\frac{P^*}{3}(10R^{*8}+80R^{*6}+522R^{*4}+390R^{*2}+60)\right]$$

$$g(R^*,P^*)=\frac{(1-R^{*2})^9}{5R^{*6}-117R^{*4}-99R^{*2}-15}\left[-1+\frac{P^*(1+2R^{*2})}{3}\right] \qquad (C-3)$$

and the reduced quantities are defined as;

$$r^*=r/R$$

$$R^*=R/r_m \qquad (C-4)$$

$$P^*=C/\varepsilon r_m^4$$

$$V^*(r^*)=V(r^*)/\varepsilon$$

where $-\varepsilon$ is the minimum of interaction potential $V(r)$ and r_m is the position of this minimum. P^* in above equations is the ratio of polarization term to the value of total potential at $r=r_m$. Therefore for $P^*=0$ Eq.C-2 gives the interaction potential between the neutral drop and the vapor atom. The value of $P^*=0$ can also be used as an approximation for very large charged drops where the polarization term is small compared to van der Waals interactions. Because this value of P^* might have more

applications we have included it in our calculations even though it is not useful for us.

Thermally averaged momentum transfer cross section $\Omega^{(1,1)}$ is defined as ;

$$\Omega^{(1,1)}(T)=\frac{1}{2(kT)^3}\int_0^\infty Q^{(1)}(E)\, e^{-E/kT}\, E^2\, dE \qquad (C\text{-}5)$$

where E is the relative energy of incident atom and $Q^{(1)}(E)$ is the transport cross section. In terms of the reduced quantities;

$$\Omega^{*(1,1)}(T^*)=\frac{1}{2T^{*3}}\int_0^\infty e^{-E^*/T^*}\, E^{*2}\, Q^{*(1)}(E^*)\, dE^* \qquad (C\text{-}6)$$

where $T^*=kT/\varepsilon$

$E^*=E/\varepsilon$

$\Omega^{*(1,1)}=\Omega^{(1,1)}/\pi R^2$ (C-7)

$Q^{*(1)}=Q^{(1)}/\pi R^2$

If the transport cross section, $Q^{(1)}$, is known then $\Omega^{(1,1)}$ can be calculated from Eq.C-6. $Q^{(1)}$ depends on both the nature and the mechanics of scattering between the drop and the incident atom. We have calculated the transport cross section both in elastic and in inelastic scattering models. In elastic model the quantum effects are also included.

1. Elastic Model

i.Classical case:

For this case the reduced diffusion cross section $Q^{*(1)}$ is given by;

$$Q^{*(1)} = 2\int_0^{\infty} (1-\cos\theta)\, b^*\, db^* \qquad (C\text{-}8)$$

where reduced impact parameter $b^*=b/R$, and deflection angle θ is

$$\theta = \pi - rb^*\int_{r_a^*}^{\infty} [1-b^{*2}/r^{*2}-V^*(r^*)/E^*]^{-1/2} / r^{*2}\, dr^* \qquad (C\text{-}9)$$

where $r_a^*=r_a/R$, the minimum approach, r_a, is the outmost zero of $1-b/r^2-V(r)/E$.

$\Omega^{*(1,1)}$ is calculated by numerical integration of three collision integrals given by Equations C-6, C-8 and C-9. The ranges and increments of parameters chosen for R^*,P^*,E^* and T^* are given in Table C-1. The estimated error in $Q^{*(1)}$ and $\Omega^{*(1,1)}$ are within 0.05% and 0.1% respectively. The results obtained for diffusion cross sections are listed in Table C-2. In above calculations the method described by O'Hara and Smith is used .

ii.Quantum mechanical case:

For quantum mechanical case $\Omega^{*(1,1)}$ can still be calculated by Eq.C-6. The main difference is the occurence of an extra parameter corresponding to the de Broglie wavelength.

The reduced wavelength is defined as

$$\Lambda^* = h/R(2m_r\varepsilon)^{1/2} \qquad (C\text{-}10)$$

where m_r is the reduced mass of drop-atom system. Λ^*, sometimes called the de Boer parameter, is a measure of the quantum nature of the system. It is zero for a classical system and increases with the quantum effects.

The reduced diffusion cross section is

$$Q^{*(1)} = \frac{\Lambda^{*2}}{\pi^2 E^{*2}} \sum_{\ell=0}^{\infty} (\ell+1)\, \mathrm{Sin}^2(\delta_\ell - \delta_{\ell+1}) \qquad (C\text{-}11)$$

where δ_ℓ is the phase shift for quantum number ℓ. δ_ℓ's are calculated by solving the Schoredinger equation numerically.

Effective reduced potential

$$V^*_{eff}(r^*) = V^*(r^*) + \frac{\Lambda^{*2}}{\pi\pi^2} \frac{\ell(\ell+1)}{r^{*2}} \qquad (C\text{-}12)$$

has an horizontal inflection point at $\ell=\ell_0$ which corresponds to $V^*_{eff}(r^*)=E^*_0$. For $\ell>\ell_0$ $V^*_{eff}(r^*)$ has no dip. Quantum effects become increasingly more important for $E^* < E^*_0$ for which the wavelength of the incident atom becomes comparable to the characteristic length of the potential. We have made use of two different methods, namely JWKB and Noumerov methods, to calculate the phase shifts for $E^* < E^*_0$. In this range of energy there is a value of ℓ, ℓ_c, for which $V^*_{eff}(r^*) = E^*_c$ is a maximum, with $\partial V^*_{eff}(r^*)/\partial r^*=0$. (See Fig.C-1.)

JWKB method is a semiclassical method which ignores the reflection and the transfer of the incident atom from and through the energy barrier of V^*_{eff} for $E^* > E^*_c$ and $E^* < E^*_c$ respectively. Hence this approximate method is not good for ℓ near ℓ_c. Noumerov method gives almost exact phase shifts for all values of ℓ. For each incident energy, E^*, we have calculated the phase shifts around ℓ_c in Numerov method and rest of the phase shifts are calculated in JWKB method. The error in $Q^{*(1)}$ is estimated to be within 0.3%. For $E^* > E^*_0$ the values of $Q^{*(1)}$'s, calculated by classical and the quantum mechanical approaches, are found to be the same within the error limits of each calculation. Therefore classical $Q^{*(1)}$'s are used to calculate $\Omega^{*(1,1)}$ in this energy range. The values of $Q^{*(1)}$'s are listed in Table C-3.

The ranges and increments chosen for R^*, P^*, Λ^* and E^* are tabulated in Table C-1.

2. Inelastic Model

In this model we assumed that every atom which does "touch" the drop is absorbed and then reemitted randomly with the same energy to maintain the thermal equilibrium of the system. This corresponds to $1-\cos\theta=1$ in Eq.C-8. Furthermore we assumed that an atom "touches" the drop if its closest distance of approach is smaller than the position of the minimum of the potential V(r). The atoms which do not "touch" the drop are assumed to be scattered elastically. The method of calculation is the same as explained in elastic classical model. Calculated $Q^{*(1)}$ values are listed in Table C-4.

3. Calculation of experimental radii

To be able to make use of the results of above calculations, namely $\Omega^{*(1,1)}$'s; for each experimental temperature, the drop radius has changed from 6A to 15A by 1A steps. The parameters R^*_{exp}, P^*_{exp}, Λ^*_{exp} and T^*_{exp} were calculated for each radius. Successive interpolations of $\Omega^{*(1,1)}$ over T^*, P^* (and Λ^* in quantum mechanical case) are used to calculate $\Omega^{(1,1)}$ as function of R for every experimental temperature. Comparison of these $\Omega^{*(1,1)}$'s with experimental cross sections obtained directly from the mobilities gives the "experimental" drop radii.

TABLE C-1

The ranges and the increments chosen for the parameters R^*, P^*, Λ^*, E^* and T^* in classical and quantum mechanical calculations of $\Omega^{(1,1)}$.

CLASSICAL

x	Range of x	x_n	
R^*	0.7-0.9	$0.1(\cos\frac{n\pi}{4}+1)+0.7$	, n=0,1,2,3,4
P^*	0.0-0.5	$0.25(\cos\frac{n\pi}{4}+1)$	, n=0,1,2,3,4
E_1^*	0.001-E_o^*	$E_o^*(\frac{0.001}{E_o^*})^{n/16}$	, n=0,1,2,...,16
E_2^*	E_o^*-10E_o^*	$10E_o^*(0.1)^{n/16}$	, n=0,1,2,...,16
E_3^*	10E_o^*-100E_o^*	$100E_o^*(0.1)^{n/4}$	, n=0,1,2,...,4
T^*	0.13-0.80	$0.385(\cos\frac{n\pi}{4}+1)+0.13$,	n=0,1,2,3,4

TABLE C-1 continue

QUANTUM MECHANICAL

x	Range of x	x_n	
R^*	0.7-0.9	$0.1(\cos\frac{n\pi}{2}+1)+0.7$	, n=0,1,2
P^*	0.0-0.5	$0.25(\cos\frac{n\pi}{2}+1)+0.7$	, n=0,1,2
Λ^*	0.3-1.0	$0.35(\cos\frac{n\pi}{2}+1)+0.3$	,n+0,1,2
E_1^*	same as the classical case ...		
E_2^*	same as the classical case ...		
E_3^*	same as the classical case ...		
T^*	same as the classical case ...		

The total range of E^* is $0.001\text{-}100E_o^*$ where E_o^* is the value of the effective potential at the horizontal inflection point.

TABLE C-2

The transport cross sections, $Q^{(1)}$'s, calculated in elastic classical model.

$R_0^*=0.9$, $E_n^*=E_0^*(0.001/E_0^*)^{n/16}$

	P_n^*				
E_n^*	n=0	n=1	n=2	n=3	n=4
n=0	1.311	1.290	1.256	1.235	1.228
n=1	1.411	1.372	1.311	1.274	1.262
n=2	1.567	1.499	1.389	1.323	1.304
n=3	1.826	1.705	1.506	1.390	1.356
n=4	2.241	2.039	1.689	1.478	1.420
n=5	2.856	2.556	1.977	1.602	1.499
n=6	3.687	3.293	2.427	1.778	1.595
n=7	4.774	4.273	3.090	2.030	1.712
n=8	6.190	5.555	4.006	2.396	1.853
n=9	8.017	7.228	5.240	2.931	2.021
n=10	10.397	9.398	6.865	3.697	2.230
n=11	13.482	12.230	8.988	4.760	2.478
n=12	17.472	15.907	11.786	6.208	2.771
n=13	22.660	20.723	15.437	8.144	3.129
n=14	29.368	26.942	20.237	10.704	3.556
n=15	38.061	35.063	26.473	14.086	4.054
n=16	49.224	45.499	34.641	18.515	4.644

TABLE C-2 continue

$R_0^* = 0.9$, $E_n^* = 10E_0^*(0.1)^{n/16}$

E_n^*	P_n^* n=0	n=1	n=2	n=3	n=4
n=0	1.146	1.145	1.143	1.141	1.140
n=1	1.150	1.148	1.145	1.144	1.143
n=2	1.154	1.152	1.149	1.146	1.146
n=3	1.158	1.156	1.152	1.150	1.149
n=4	1.163	1.160	1.156	1.153	1.152
n=5	1.169	1.165	1.160	1.157	1.155
n=6	1.174	1.170	1.164	1.160	1.159
n=7	1.181	1.176	1.169	1.165	1.163
n=8	1.186	1.182	1.174	1.169	1.167
n=9	1.195	1.190	1.180	1.174	1.171
n=10	1.205	1.198	1.186	1.179	1.176
n=11	1.216	1.207	1.194	1.185	1.182
n=12	1.229	1.219	1.202	1.192	1.188
n=13	1.244	1.232	1.213	1.200	1.196
n=14	1.262	1.248	1.224	1.209	1.204
n=15	1.284	1.267	1.238	1.220	1.214
n=16	1.309	1.289	1.255	1.233	1.227

$R_0^* = 0.9$, $E_0^* = 100E_0^*(0.1)^{n/4}$

E_n^*	P_n^* n=0	n=1	n=2	n=3	n=4
n=0	1.106	1.106	1.106	1.106	1.106
n=1	1.115	1.114	1.114	1.114	1.114
n=2	1.123	1.123	1.122	1.121	1.121
n=3	1.133	1.133	1.131	1.130	1.130
n=4	1.146	1.145	1.142	1.141	1.140

TABLE C-2 continue

$R_1^* = 0.8707$, $E_n^* = E_0^*(0.001/E_0^*)^{n/16}$

E_n^*	P_n^* n=0	n=1	n=2	n=3	n=4
n=0	1.449	1.419	1.370	1.339	1.330
n=1	1.587	1.534	1.451	1.398	1.381
n=2	1.796	1.706	1.559	1.468	1.442
n=3	2.121	1.972	1.718	1.561	1.515
n=4	2.610	2.377	1.955	1.685	1.607
n=5	3.302	2.970	2.309	1.852	1.718
n=6	4.228	3.789	2.829	2.079	1.855
n=7	5.431	4.872	3.569	2.393	2.019
n=8	6.988	6.286	4.572	2.829	2.218
n=9	8.993	8.117	5.917	3.437	2.453
n=10	11.575	10.475	7.679	4.275	2.741
n=11	14.906	13.544	9.974	5.419	3.079
n=12	19.191	17.480	12.961	6.947	3.489
n=13	24.688	22.560	16.852	8.992	3.981
n=14	31.792	29.163	21.902	11.676	4.552
n=15	40.893	37.668	28.503	15.201	5.237
n=16	52.695	48.635	36.965	19.796	6.063

$R_1^* = 0.8707$, $E_n^* = 10E_0^*(0.1)^{n/16}$

E_n^*	P_n^* n=0	n=1	n=2	n=3	n=4
n=0	1.204	1.202	1.199	1.197	1.196
n=1	1.210	1.208	1.204	1.201	1.200
n=2	1.215	1.212	1.208	1.206	1.205
n=3	1.221	1.219	1.213	1.210	1.209
n=4	1.228	1.225	1.219	1.214	1.213
n=5	1.235	1.231	1.225	1.220	1.218
n=6	1.243	1.238	1.230	1.225	1.223
n=7	1.253	1.247	1.237	1.231	1.229
n=8	1.263	1.257	1.245	1.238	1.235
n=9	1.275	1.267	1.254	1.246	1.242
n=10	1.289	1.280	1.264	1.253	1.250
n=11	1.306	1.294	1.274	1.262	1.258
n=12	1.325	1.311	1.287	1.273	1.268
n=13	1.349	1.331	1.303	1.285	1.280
n=14	1.376	1.355	1.322	1.300	1.293
n=15	1.410	1.385	1.344	1.318	1.310
n=16	1.447	1.418	1.368	1.339	1.330

TABLE C-2 continue

$R_1^* = 0.8707$, $E_n^* = 100 E_0^* (0.1)^{n/4}$

E_n^*	P_n^* n=0	n=1	n=2	n=3	n=4
n=0	1.148	1.148	1.148	1.148	1.148
n=1	1.159	1.159	1.158	1.158	1.158
n=3	1.186	1.185	1.184	1.182	1.182
n=4	1.204	1.202	1.199	1.197	1.196

$R_2^* = 0.8000$, $E_n^* = E_0^* (0.001/E_0^*)^{n/16}$

E_n^*	P_n^* n=0	n=1	n=2	n=3	n=4
n=0	1.872	1.820	1.729	1.674	1.655
n=1	2.120	2.035	1.887	1.789	1.758
n=2	2.461	2.327	2.087	1.927	1.878
n=3	2.942	2.738	2.361	2.103	2.023
n=4	3.606	3.311	2.737	2.328	2.199
n=5	4.497	4.091	3.254	2.616	2.412
n=6	5.662	5.130	3.958	2.988	2.668
n=7	7.149	6.483	4.905	3.471	2.975
n=8	9.095	8.231	6.155	4.099	3.341
n=9	11.559	10.475	7.796	4.916	3.773
n=10	14.696	13.350	9.924	5.967	4.289
n=11	18.701	17.011	12.672	7.380	4.890
n=12	23.754	21.689	16.205	9.223	5.629
n=13	30.270	27.661	20.747	11.594	6.496
n=14	38.430	35.256	26.579	14.684	7.520
n=15	48.890	44.932	34.106	18.670	8.723
n=16	62.224	57.409	43.694	23.827	10.133

TABLE C-2 continue

$R_2^* = 0.8000$, $E_n^* = 10E_0^*(0.1)^{n/16}$

E_n^*	P_n^* n=0	n=1	n=2	n=3	n=4
n=0	1.375	1.372	1.368	1.363	1.363
n=1	1.385	1.381	1.376	1.372	1.370
n=2	1.395	1.391	1.384	1.379	1.378
n=3	1.407	1.402	1.394	1.388	1.386
n=4	1.419	1.414	1.404	1.398	1.386
n=5	1.434	1.427	1.415	1.408	1.405
n=6	1.451	1.442	1.428	1.419	1.415
n=7	1.469	1.459	1.436	1.430	1.427
n=8	1.490	1.479	1.458	1.444	1.439
n=9	1.514	1.501	1.477	1.460	1.454
n=10	1.544	1.527	1.498	1.477	1.471
n=11	1.578	1.558	1.522	1.498	1.491
n=12	1.619	1.595	1.552	1.522	1.513
n=13	1.674	1.639	1.587	1.552	1.541
n=14	1.734	1.697	1.630	1.587	1.574
n=15	1.806	1.762	1.680	1.630	1.614
n=16	1.876	1.825	1.731	1.673	1.654

$R_2^* = 0.8000$, $E_n^* = 100E_0^*(0.1)^{n/4}$

E_n^*	P_n^* n=0	n=1	n=2	n=3	n=4
n=0	1.272	1.272	1.272	1.271	1.271
n=1	1.293	1.292	1.291	1.291	1.290
n=2	1.316	1.315	1.313	1.312	1.312
n=3	1.342	1.341	1.338	1.336	1.335
n=4	1.375	1.372	1.367	1.363	1.362

TABLE C-2 continue

$R_3^* = 0.7293$, $E_n^* = E_0^*(0.001/E_0^*)^{n/16}$

E_n^*	P_n^* n=0	n=1	n=2	n=3	n=4
n=0	2.458	2.383	2.244	2.144	2.114
n=1	2.840	2.724	2.506	2.350	2.302
n=2	3.333	3.159	2.826	2.585	2.508
n=3	3.991	3.739	3.242	2.873	2.754
n=4	4.862	4.508	3.787	3.232	3.050
n=5	5.998	5.521	4.501	3.679	3.403
n=6	7.463	6.836	5.435	4.237	3.822
n=7	9.338	8.526	6.652	4.937	4.321
n=8	11.719	10.687	8.223	5.819	4.911
n=9	14.733	13.443	10.249	6.922	5.605
n=10	18.561	16.943	12.843	8.329	6.425
n=11	23.395	21.384	16.168	10.106	7.396
n=12	29.480	26.995	20.408	12.377	8.533
n=13	37.166	34.119	25.796	15.272	9.877
n=14	46.871	43.064	32.667	18.934	11.459
n=15	59.102	54.418	41.390	23.623	13.320
n=16	74.656	68.722	52.471	29.589	15.496

$R_3^* = 0.7293$, $E_n^* = 10E_0^*(0.1)^{n/16}$

E_n^*	P_n^* n=0	n=1	n=2	n=3	n=4
n=0	1.603	1.599	1.592	1.585	1.584
n=1	1.618	1.614	1.606	1.599	1.596
n=2	1.636	1.630	1.620	1.612	1.610
n=3	1.655	1.648	1.636	1.626	1.624
n=4	1.676	1.669	1.653	1.643	1.639
n=5	1.699	1.691	1.673	1.660	1.656
n=6	1.727	1.716	1.695	1.680	1.674
n=7	1.757	1.744	1.720	1.701	1.695
n=8	1.793	1.778	1.748	1.725	1.719
n=9	1.841	1.816	1.780	1.753	1.745
n=10	1.893	1.868	1.818	1.785	1.776
n=11	1.955	1.925	1.869	1.824	1.812
n=12	2.029	1.993	1.925	1.874	1.860
n=13	2.130	2.075	1.993	1.932	1.914
n=14	2.241	2.186	2.074	2.001	1.979
n=15	2.365	2.301	2.166	2.081	2.057
n=16	2.463	2.396	2.235	2.152	2.123

TABLE C-2 continue

$R_3^* = 0.7293$, $E_n^* = 100E_o^*(0.1)^{n/4}$

E_n^*	P_n^* n=0	n=1	n=2	n=3	n=4
n=0	1.434	1.436	1.436	1.435	1.435
n=1	1.469	1.469	1.468	1.467	1.467
n=2	1.507	1.506	1.503	1.501	1.501
n=3	1.550	1.548	1.544	1.540	1.540
n=4	1.603	1.599	1.592	1.586	1.584

$R_4^* = 0.7000$, $E_n^* = E_0^*(0.001/E_0^*)^{n/16}$

E_n^*	P_n^* n=0	n=1	n=2	n=3	n=4
n=0	2.767	2.678	2.514	2.397	2.357
n=1	3.216	3.082	2.832	2.651	2.588
n=2	3.786	3.589	3.213	2.936	2.840
n=3	4.533	4.251	3.700	3.283	3.140
n=4	5.507	5.119	4.329	3.710	3.496
n=5	6.768	6.248	5.142	4.239	3.921
n=6	8.386	7.701	6.194	4.893	4.424
n=7	10.445	9.565	7.546	5.706	5.021
n=8	13.051	11.935	9.284	6.716	5.724
n=9	16.352	14.945	11.506	7.976	6.553
n=10	20.520	18.751	14.340	9.550	7.529
n=11	25.778	23.584	17.954	11.522	8.639
n=12	32.373	29.671	22.554	14.035	10.024
n=13	40.680	37.321	28.387	17.200	11.619
n=14	51.134	47.000	35.782	21.196	13.476
n=15	64.309	59.210	45.177	26.250	15.667
n=16	80.797	74.552	57.018	32.590	18.205

TABLE C-2 continue

$R_4^* = 0.7000$, $E_n^* = 10E_0^*(0.1)^{n/16}$

E_n^*	P_n^* n=0	n=1	n=2	n=3	n=4
n=0	1.719	1.711	1.706	1.699	1.696
n=1	1.738	1.732	1.723	1.715	1.711
n=2	1.758	1.752	1.740	1.731	1.727
n=3	1.784	1.773	1.759	1.749	1.744
n=4	1.808	1.799	1.780	1.768	1.763
n=5	1.838	1.826	1.806	1.789	1.783
n=6	1.871	1.857	1.833	1.814	1.805
n=7	1.909	1.893	1.863	1.842	1.833
n=8	1.954	1.934	1.898	1.872	1.862
n=9	2.006	1.982	1.939	1.900	1.895
n=10	2.078	2.048	1.987	1.949	1.934
n=11	2.157	2.119	2.043	1.998	1.980
n=12	2.250	2.205	2.123	2.056	2.036
n=13	2.359	2.307	2.210	2.137	2.110
n=14	2.516	2.447	2.312	2.225	2.193
n=15	2.664	2.587	2.425	2.327	2.290
n=16	2.770	2.693	2.539	2.410	2.370

$R_4^* = 0.7000$, $E_n^* = 100E_0^*(0.1)^{n/4}$

E_n^*	P_n^* n=0	n=1	n=2	n=3	n=4
n=0	1.520	1.520	1.519	1.519	1.518
n=1	1.560	1.559	1.558	1.556	1.556
n=2	1.604	1.603	1.600	1.598	1.597
n=3	1.656	1.653	1.649	1.645	1.643
n=4	1.720	1.715	1.706	1.700	1.697

TABLE C-3

The transport cross sections, $Q^{(1)}$'s, calculated in elastic quantum mechanical model.

$R_0^* = 0.9$, $p_0^* = 0.5$				$R_0^* = 0.9$, $p_1^* = 0.25$		
	Λ_n^*			Λ_n^*		
E_n^*	n=0	n=1	n=2	n=0	n=1	n=2
n=0	1.335	1.361	1.368	1.250	1.283	1.300
n=1	1.463	1.479	1.503	1.369	1.381	1.395
n=2	1.680	1.743	1.740	1.490	1.525	1.530
n=3	2.104	2.052	2.033	1.729	1.766	1.668
n=4	2.859	2.785	2.231	1.401	1.426	1.977
n=5	2.135	3.920	3.040	1.472	1.626	2.524
n=6	3.052	4.152	3.231	1.660	2.156	2.585
n=7	4.891	6.273	5.229	1.970	3.161	2.567
n=8	8.229	6.551	6.389	2.388	4.897	3.287
n=9	14.391	9.934	6.075	3.420	8.337	5.414
n=10	15.598	4.930	11.585	5.538	9.950	9.670
n=11	21.659	12.274	19.480	10.681	15.483	9.583
n=12	28.203	20.369	10.790	18.189	16.670	9.932
n=13	20.232	34.021	25.992	30.649	4.965	17.005
n=14	8.993	62.747	39.509	51.404	5.801	25.984
n=15	6.412	106.440	65.917	61.167	7.616	53.332
n=16	9.685	56.432	31.832	85.361	8.451	18.977

TABLE C-3 continue

$R_0^* = 0.9$, $p_2^* = 0.0$

E_n^*	Λ_n^* n=0	n=1	n=2
n=0	1.255	1.255	1.273
n=1	1.296	1.329	1.338
n=2	1.407	1.403	1.428
n=3	1.482	1.528	1.522
n=4	1.280	1.211	1.612
n=5	1.332	1.210	1.867
n=6	1.407	1.222	2.423
n=7	1.509	1.232	1.915
n=8	1.657	1.246	1.762
n=9	1.862	1.291	1.857
n=10	2.135	1.353	1.943
n=11	2.463	1.448	2.058
n=12	2.780	1.561	2.193
n=13	3.032	1.606	2.391
n=14	3.200	1.580	2.617
n=15	3.315	1.528	2.924
n=16	3.383	1.478	3.280

$R_1^* = 0.8$, $p_0^* = 0.5$

E_n^*	Λ_n^* n=0	n=1	n=2
n=0	1.962	1.955	1.983
n=1	2.370	2.368	2.258
n=2	3.059	2.912	2.447
n=3	4.140	3.492	2.748
n=4	4.967	3.836	3.809
n=5	5.687	4.443	5.136
n=6	9.053	5.720	6.177
n=7	11.928	7.027	7.632
n=8	9.755	9.356	10.613
n=9	5.402	14.407	14.912
n=10	7.616	21.149	17.807
n=11	8.402	34.048	26.166
n=12	11.923	14.763	31.575
n=13	16.188	13.693	22.830
n=14	26.681	21.683	38.784
n=15	34.259	37.026	71.711
n=16	63.806	38.069	77.174

$R_1^* = 0.8$, $p_1^* = 0.25$

E_n^*	Λ_n^* n=0	n=1	n=2
n=0	1.782	1.801	1.812
n=1	2.042	2.079	2.009
n=2	2.496	2.490	2.169
n=3	3.228	3.926	2.199
n=4	4.004	3.259	2.607
n=5	3.254	4.785	3.646
n=6	4.830	4.048	4.698
n=7	7.711	3.778	5.090
n=8	12.088	4.154	5.836
n=9	24.304	5.353	7.324
n=10	11.280	6.951	12.265
n=11	10.316	14.035	20.251
n=12	7.962	24.587	16.023
n=13	14.979	36.167	20.721
n=14	15.745	68.121	33.283
n=15	6.513	82.634	54.340
n=16	6.794	50.643	83.772

$R_1^* = 0.8$, $p_2^* = 0.0$

E_n^*	Λ_n^* n=0	n=1	n=2
n=0	1.688	1.710	1.731
n=1	1.890	1.927	1.893
n=2	2.252	2.243	1.904
n=3	2.696	2.642	2.158
n=4	3.283	2.885	2.037
n=5	1.824	3.531	2.365
n=6	2.045	4.117	2.946
n=7	2.292	6.368	3.937
n=8	2.750	4.287	5.075
n=9	3.531	3.521	4.422
n=10	6.212	3.728	3.279
n=11	7.126	4.210	3.786
n=12	8.446	4.730	3.456
n=13	17.356	5.338	3.717
n=14	34.186	6.024	3.834
n=15	60.969	6.664	3.918
n=16	96.472	7.140	4.064

TABLE C-3 continue

$R_2^* = 0.7$, $p_0^* = 0.5$

E_n^*	Λ_n^* n=0	n=1	n=2
n=0	2.975	2.997	3.017
n=1	3.840	3.825	3.390
n=2	5.262	4.154	3.778
n=3	5.605	4.390	5.258
n=4	6.151	4.533	6.427
n=5	5.251	6.548	7.382
n=6	5.041	9.588	9.999
n=7	15.014	13.955	12.527
n=8	11.245	15.616	15.596
n=9	13.519	23.862	17.316
n=10	33.377	13.279	18.193
n=11	37.574	25.090	26.288
n=12	63.407	39.966	45.988
n=13	110.015	61.002	28.938
n=14	90.600	97.770	67.338
n=15	69.687	75.449	116.604
n=16	54.570	66.186	144.950

$R_2^* = 0.7$, $p_1^* = 0.25$

E_n^*	Λ_n^* n=0	n=1	n=2
n=0	2.645	2.675	2.652
n=1	3.319	3.259	2.881
n=2	4.209	3.932	3.046
n=3	4.947	3.687	4.105
n=4	5.905	3.803	4.542
n=5	6.633	4.196	5.510
n=6	5.799	6.057	6.780
n=7	9.432	9.351	9.064
n=8	9.186	11.787	10.122
n=9	5.704	19.076	9.808
n=10	7.584	17.784	18.965
n=11	8.581	38.868	27.447
n=12	13.888	10.410	17.167
n=13	19.971	11.633	27.220
n=14	29.059	16.786	47.432
n=15	40.412	24.573	76.008
n=16	75.665	47.556	98.872

$R_2^* = 0.7$, $p_2^* = 0.0$

E_n^*	Λ_n^* n=0	n=1	n=2
n=0	2.459	2.475	2.496
n=1	2.925	2.948	2.610
n=2	3.617	3.237	2.936
n=3	4.309	3.294	3.308
n=4	5.331	3.415	3.939
n=5	6.061	3.283	4.275
n=6	6.895	3.142	4.246
n=7	5.809	3.448	5.422
n=8	13.012	4.480	7.233
n=9	5.361	4.630	10.429
n=10	6.087	6.434	8.842
n=11	6.920	10.080	7.293
n=12	7.748	12.139	6.497
n=13	8.667	22.282	9.497
n=14	9.438	36.066	15.945
n=15	10.011	53.194	23.029
n=16	10.364	78.026	34.079

TABLE C-4

The transport cross sections, $Q^{(1)}$'s, calculated in inelastic classical model .

$R_0^*=0.9$, $E_n^*=E_0^*(0.001/E_0^*)^{n/16}$

E_0^*	P_n^* n=0	n=1	n=2	n=3	n=4
n=0	1.598	1.558	1.490	1.445	1.432
n=1	1.774	1.710	1.602	1.533	1.517
n=2	2.034	1.929	1.750	1.633	1.596
n=3	2.418	2.250	1.953	1.757	1.695
n=4	2.929	2.722	2.242	1.914	1.810
n=5	3.760	3.393	2.662	2.119	1.945
n=6	4.784	4.316	3.266	2.393	2.105
n=7	6.097	5.510	4.111	2.767	2.293
n=8	7.781	7.046	5.246	3.284	2.516
n=9	9.947	9.028	6.731	4.000	2.780
n=10	12.735	11.585	8.664	4.982	3.093
n=11	16.326	14.892	11.791	6.307	3.466
n=12	20.955	19.166	14.451	8.069	3.909
n=13	26.906	24.691	18.710	10.389	4.438
n=14	34.627	31.851	24.258	13.434	5.069
n=15	44.535	41.111	31.487	17.423	5.823
n=16	57.393	53.119	40.912	22.657	6.724

TABLE C-4 continue

$R_0^* = 0.9$, $E_n^* = 10E_0^*(0.1)^{n/16}$

E_n^*	p_n^* n=0	n=1	n=2	n=3	n=4
n=0	1.267	1.264	1.258	1.254	1.253
n=1	1.272	1.268	1.261	1.257	1.255
n=2	1.278	1.274	1.266	1.260	1.259
n=3	1.284	1.279	1.271	1.264	1.262
n=4	1.292	1.287	1.276	1.269	1.267
n=5	1.302	1.294	1.283	1.275	1.272
n=6	1.313	1.304	1.290	1.281	1.278
n=7	1.325	1.315	1.299	1.288	1.284
n=8	1.339	1.328	1.310	1.297	1.292
n=9	1.356	1.343	1.321	1.307	1.302
n=10	1.376	1.361	1.335	1.318	1.313
n=11	1.400	1.382	1.352	1.332	1.326
n=12	1.427	1.407	1.371	1.348	1.340
n=13	1.460	1.435	1.393	1.367	1.358
n=14	1.497	1.468	1.420	1.388	1.378
n=15	1.541	1.508	1.450	1.414	1.402
n=16	1.591	1.551	1.485	1.443	1.430

$R_0^* = 0.9$, $E_n^* = 100E_0^*(0.1)^{n/4}$

E_n^*	p_n^* n=0	n=1	n=2	n=3	n=4
n=0	1.238	1.238	1.237	1.237	1.236
n=1	1.240	1.240	1.239	1.238	1.238
n=2	1.245	1.244	1.242	1.241	1.240
n=3	1.253	1.251	1.248	1.245	1.245
n=4	1.267	1.263	1.258	1.254	1.253

TABLE C-4 continue

$R_1^* = 0.8707$, $E_n^* = E_0^*(0.001/E_0^*)^{n/16}$

E_n^*	P_n^* n=0	n=1	n=2	n=3	n=4
n=0	1.821	1.768	1.678	1.623	1.604
n=1	2.046	1.965	1.826	1.733	1.704
n=2	2.371	2.243	2.018	1.869	1.821
n=3	2.834	2.636	2.278	2.033	1.954
n=4	3.480	3.190	2.635	2.239	2.111
n=5	4.351	3.954	3.132	2.502	2.294
n=6	5.486	4.971	3.821	2.844	2.510
n=7	6.935	6.287	4.757	3.296	2.764
n=8	8.787	7.977	6.000	3.898	3.065
n=9	11.152	10.143	7.620	4.703	3.420
n=10	14.180	12.922	9.718	5.779	3.841
n=11	18.054	16.489	12.430	7.207	4.339
n=12	23.011	21.067	15.935	9.087	4.931
n=13	29.355	26.947	20.466	11.546	5.634
n=14	37.490	34.451	26.323	14.753	6.470
n=15	47.871	44.215	33.871	18.929	7.464
n=16	61 173	56.610	43.696	24.363	8.648

$R_1^* = 0.8707$, $E_n^* = 10E_0^*(0.1)^{n/16}$

E_n^*	P_n^* n=0	n=1	n=2	n=3	n=4
n=0	1.363	1.359	1.351	1.346	1.344
n=1	1.370	1.365	1.356	1.350	1.348
n=2	1.377	1.372	1.362	1.355	1.353
n=3	1.387	1.380	1.369	1.361	1.358
n=4	1.398	1.389	1.376	1.368	1.364
n=5	1.411	1.401	1.386	1.375	1.371
n=6	1.425	1.415	1.397	1.384	1.380
n=7	1.443	1.430	1.401	1.394	1.389
n=8	1.463	1.449	1.423	1.406	1.401
n=9	1.487	1.470	1.440	1.421	1.414
n=10	1.515	1.495	1.460	1.438	1.430
n=11	1.548	1.524	1.483	1.457	1.448
n=12	1.586	1.558	1.511	1.480	1.470
n=13	1.632	1.599	1.544	1.506	1.495
n=14	1.685	1.647	1.582	1.538	1.524
n=15	1.747	1.702	1.626	1.576	1.559
n=16	1.815	1.763	1.674	1.616	1.598

TABLE C-4 continue

$R_1^* = 0.8707$, $E_n^* = 100E_0^*(0.1)^{n/4}$

E_n^*	P_n^* n=0	n=1	n=2	n=3	n=4
n=0	1.323	1.323	1.322	1.322	1.322
n=1	1.327	1.326	1.325	1.324	1.324
n=2	1.333	1.331	1.329	1.328	1.328
n=3	1.343	1.341	1.337	1.334	1.333
n=4	1.363	1.358	1.351	1.346	1.344

$R_2^* = 0.8000$, $E_n^* = E_0^*(0.001/E_0^*)^{n/16}$

E_n^*	P_n^* n=0	n=1	n=2	n=3	n=4
n=0	2.478	2.395	2.247	2.144	2.111
n=1	2.819	2.701	2.484	2.332	2.283
n=2	3.307	3.131	2.802	2.567	2.491
n=3	3.956	3.701	3.210	2.849	2.730
n=4	4.812	4.457	3.743	3.194	3.010
n=5	5.923	5.448	4.440	3.620	3.336
n=6	7.346	6.731	5.355	4.150	3.719
n=7	9.137	8.373	6.547	4.818	4.167
n=8	11.448	10.467	8.091	5.664	4.694
n=9	14.350	13.124	10.077	6.741	5.314
n=10	18.018	16.497	12.625	8.120	6.044
n=11	22.648	20.779	15.879	9.886	6.906
n=12	28.541	26.209	20.037	12.150	7.921
n=13	35.955	33.103	25.347	15.055	9.118
n=14	45.334	41.853	32.124	18.781	10.531
n=15	57.270	52.967	40.780	23.560	12.191
n=16	72.456	67.080	51.787	29.689	14.171

TABLE C-4 continue

$R_2^* = 0.8000$, $E_n^* = 10E_0^*(0.1)^{n/16}$

E_n^*	P_n^* n=0	n=1	n=2	n=3	n=4
n=0	1.640	1.634	1.622	1.613	1.610
n=1	1.652	1.645	1.631	1.621	1.617
n=2	1.667	1.658	1.641	1.630	1.626
n=3	1.684	1.674	1.654	1.641	1.636
n=4	1.703	1.691	1.669	1.654	1.648
n=5	1.726	1.712	1.686	1.668	1.662
n=6	1.754	1.737	1.707	1.685	1.679
n=7	1.786	1.767	1.731	1.706	1.698
n=8	1.824	1.801	1.759	1.730	1.720
n=9	1.868	1.841	1.792	1.757	1.746
n=10	1.922	1.889	1.831	1.790	1.777
n=11	1.984	1.946	1.878	1.829	1.814
n=12	2.059	2.013	1.932	1.875	1.857
n=13	2.146	2.092	1.997	1.929	1.909
n=14	2.249	2.185	2.072	1.994	1.969
n=15	2.364	2.291	2.159	2.068	2.039
n=16	2.477	2.394	2.246	2.143	2.110

$R_n^* = 0.8000$, $E_n^* = 100E_0^*(0.1)^{n/4}$

E_n^*	P_n^* n=0	n=1	n=2	n=3	n=4
n=0	1.570	1.569	1.568	1.568	1.567
n=1	1.576	1.575	1.573	1.571	1.571
n=2	1.586	1.585	1.581	1.578	1.577
n=3	1.605	1.602	1.595	1.591	1.589
n=4	1.640	1.633	1.621	1.613	1.610

TABLE C-4 continue

$R_3^* = 0.7293$, $E_n^* = E_0^*(0.001/E_0^*)^{n/16}$

E_n^*	P_n^* n=0	n=1	n=2	n=3	n=4
n=0	3.345	3.027	3.234	2.867	2.818
n=1	3.818	3.368	3.665	3.146	3.076
n=2	4.494	3.844	4.276	3.516	3.408
n=3	5.361	4.437	5.056	3.954	3.791
n=4	6.471	5.185	6.056	4.479	4.236
n=5	7.883	6.132	7.322	5.115	4.754
n=6	9.670	7.336	8.955	5.890	5.359
n=7	11.924	8.846	11.009	6.840	6.067
n=8	14.759	10.810	13.603	8.011	6.895
n=9	18.324	13.276	16.873	9.463	7.864
n=10	22.800	16.399	20.991	11.271	9.001
n=11	28.422	20.353	26.174	13.531	10.333
n=12	35.486	25.359	32.704	16.364	11.896
n=13	44.357	31.670	40.923	19.929	13.730
n=14	55.504	39.696	51.271	24.421	15.883
n=15	69.505	49.840	64.303	30.095	18.408
n=16	87.114	62.569	80.715	37.273	21.379

$R_3^* = 0.7293$, $E_n^* = 10E_0^*(0.1)^{n/16}$

E_n^*	P_n^* n=0	n=1	n=2	n=3	n=4
n=0	2.003	1.994	1.977	1.964	1.960
n=1	2.022	2.012	1.992	1.977	1.972
n=2	2.046	2.034	2.010	1.993	1.987
n=3	2.073	2.059	2.032	2.011	2.004
n=4	2.104	2.088	2.056	2.033	2.025
n=5	2.142	2.123	2.085	2.058	2.049
n=6	2.186	2.164	2.120	2.087	2.077
n=7	2.239	2.212	2.160	2.121	2.110
n=8	2.301	2.269	2.208	2.162	2.148
n=9	2.375	2.337	2.226	2.210	2.194
n=10	2.463	2.418	2.333	2.269	2.249
n=11	2.568	2.515	2.413	2.337	2.314
n=12	2.693	2.629	2.509	2.418	2.391
n=13	2.840	2.765	2.622	2.514	2.483
n=14	3.010	2.922	2.753	2.627	2.590
n=15	3.196	3.095	2.900	2.756	2.712
n=16	3.357	3.244	3.034	2.871	2.821

TABLE C-4 continue

$R_3^* = 0.7293$, $E_n^* = 100E_0^*(0.1)^{n/4}$

E_n^*	P_n^* n=0	n=1	n=2	n=3	n=4
n=0	1.892	1.891	1.890	1.888	1.888
n=1	1.901	1.900	1.897	1.895	1.894
n=2	1.918	1.915	1.910	1.906	1.905
n=3	1.948	1.943	1.934	1.927	1.924
n=4	2.003	1.994	1.977	1.964	1.960

$R_4^* = 0.7000$, $E_n^* = E_0^*(0.001/E_0^*)^{n/16}$

E_n^*	P_n^* n=0	n=1	n=2	n=3	n=4
n=0	3.791	3.664	3.423	3.248	3.182
n=1	4.332	4.157	3.824	3.572	3.483
n=2	5.103	4.858	4.379	4.011	3.879
n=3	6.081	5.742	5.064	4.528	4.337
n=4	7.319	6.864	5.920	5.146	4.866
n=5	8.885	8.285	6.993	5.890	5.483
n=6	10.857	10.080	8.345	6.789	6.202
n=7	13.337	12.343	10.048	7.885	7.041
n=8	16.444	15.189	12.198	9.224	8.023
n=9	20.344	18.765	14.909	10.871	9.170
n=10	25.225	23.258	18.329	12.903	10.512
n=11	31.340	28.899	22.689	15.424	12.084
n=12	39.000	35.951	28.076	18.561	13.924
n=13	48.593	44.863	34.905	22.477	16.079
n=14	60.574	56.022	43.572	27.381	18.605
n=15	75.667	70.033	54.426	33.535	21.560
n=16	94.556	87.645	68.209	41.207	25.034

TABLE C-4 continue

$R_4^* = 0.7000$, $E_n^* = 10E_0^*(0.1)^{n/16}$

E_n^*	P_n^* n=0	n=1	n=2	n=3	n=4
n=0	2.188	2.176	2.159	2.143	2.137
n=1	2.212	2.200	2.178	2.159	2.152
n=2	2.240	2.226	2.199	2.178	2.170
n=3	2.274	2.256	2.224	2.200	2.191
n=4	2.312	2.293	2.254	2.226	2.216
n=5	2.358	2.335	2.289	2.257	2.245
n=6	2.414	2.382	2.331	2.293	2.279
n=7	2.473	2.441	2.381	2.336	2.319
n=8	2.548	2.510	2.439	2.386	2.366
n=9	2.638	2.593	2.509	2.446	2.423
n=10	2.746	2.692	2.592	2.518	2.490
n=12	3.027	2.950	2.809	2.704	2.665
n=13	3.207	3.115	2.948	2.824	2.777
n=14	3.413	3.306	3.110	2.964	2.910
n=15	3.634	3.513	3.290	3.121	3.059
n=16	3.814	3.683	3.439	3.256	3.189

$R_4^* = 0.7000$, $E_n^* = 100E_0^*(0.1)^{n/4}$

E_n^*	P_n^* n=0	n=1	n=2	n=3	n=4
n=0	2.055	2.054	2.052	2.051	2.050
n=1	2.066	2.064	2.061	2.058	2.057
n=2	2.086	2.083	2.077	2.072	2.071
n=3	2.122	2.116	2.105	2.097	2.094
n=4	2.189	2.178	2.158	2.143	2.137

BIBLIOGRAPHY

Akinci, G. and J.A.Northby; Proc. of 16th Int.Conf. on Low Temp.Phys., 575 (1982).

Atkins, K.R.; Phys.Rev. 116, 6, 1339 (1959).

Brůch, L.W. and I.J.McGee; J.Chem.Phys. 52, 5884 (1970).

Castleman, A.W.Jr., M.Holland and G.Keesee, J.Chem.Phys. 68, 4 (1978).

Dahm,A. and T.M.Sanders Jr.; J.Low Temp.Phys. 2,199 (1970).

Daniel, E.W. and E.A.Mason; The Mobility and Diffusion of Ions in Gases Ch.5 (John Wiley and Sons, New York, 1973).

Dẑidić, I. and P.Kebarle; J.Phys.Chem. 74, 1466 (1970).

Eckardt, J.R. et al.; Phys.Rev. B 16, 1944 (1977).

Edwards, D.O. and W.F.Saam; Prog. Low Temp.Phys. Vol VII A, Ch.4 (D.F.Brewer ed., North-Holland Publishing Co. 1978).

Epstein, P.S.; Phys.Rev. 23, 710 (1924).

Frenkel, J.; Kinetic Theory of Liquids (Oxford University Press, Oxford, Egnland, 1946).

Henson, B.L.; Phys.Rev. A 15, 1680 (1977).

Katz, J.L. and B.J.Ostermier; J.Chem.Phys. 47, 478 (1967).

Katz, J.L., C.J.Scoppa II, N.G.Kumar and P.Mirabel; J.Chem. Phys. 62, 448 (1975).

Northby, J.A. and G.Akinci; "Charged Droplets in Cryogenic ^{4}He Vapor", Phys.Rev.Lett. 42, 573-576 (1979).

Northby, J.A. and G.Akinci;"Ion Droplet Mobility in Cryogenic ^{4}He Vapor", J.Phys. 39, Colloq. C6, 84-85 (1978).

Northby, J.A., G.Akinci and L.S.Lagurney; "Positive Ions in Cryogenic ^{4}He Vapor", Proc. of 12th Symp. on Rarefied Gas Dynamics, 1145 (1981).

O'Hara, H. and F.J.Smith; J.Comp.Phys. 5, 328 (1970).

Russell, K.C.; J.Chem.Phys. 50, 1809 (1969).

Schwarz, K.W.; Phys.Rev. A 6, 837 (1972).

Schwarz, K.W.; Adv.Chem.Phys. 33, 1 (1974).

Smith, J.K. et al.; Phys.Rev. A 13, 1422 (1976).

Thomson,J.J.; Application of Dynamics to Physics and Chemistry, (MacMillan, London, 1888).

van Dijk, H. and M.Durieux; Physica XXIV, 920 (1958).

Volmer, M. and A.Weber; Z.Physik.Chem, Leipzig 119,277 (1926).

Wang,T.G. et al.; Phys.Rev.Lett. 30, 485 (1973).

Wilks. J.; The Properties of Liquid and Solid Helium (Clarendon Press, Oxford, 1967).

C O R R E C T I O N S

1. Add "since there is no model independent theory to compare it with. But" after line 10 on page 50.
2. Line 9 on page 51 should read "$R_\ell - R_s$ for $T < 1.9K$. The dashed lines taken from the similar graph for $T > 2.3K$ (see Fig.10) are also drawn for comparison." The existing line is incomplete.